JOURNAL OF GUIDANCE, CONTROL, AND DYNAMICS
Vol. 32, No. 1, January–February 2009

Correlation of Optical Observations of Objects in Earth Orbit

J. M. Maruskin*
San José State University, San José, California 95192-0103
D. J. Scheeres†
University of Colorado at Boulder, Boulder, Colorado 80309-0429
and
K. T. Alfriend‡
Texas A&M University, College Station, Texas 77843-3141

DOI: 10.2514/1.36398

A sequence of optical measurements of an Earth orbiting object over one track has sufficient information to determine the angles and angular rates with some degree of precision, but cannot measure the range or range rate. Despite the lack of complete state information, constraints on range and range rate can be determined by taking into account certain physical considerations, which ultimately restrict the object's state to lie within a two-dimensional submanifold of phase space. Such a region can be mapped into orbital element space and propagated in time. As the regions in question are two dimensional in nature it is possible to model them with high precision without excessive computational burden. A second observation of a space object can similarly be mapped into a similar submanifold of orbit element space and intersected with a previous observation mapped to the same epoch. If the object is the same, this intersection process yields a nonzero set which may be unique, depending on observational geometries. If the object is different, the intersection is null in general. The addition of uncertainty in the angle and angle-rate measurements yields finite regions of intersection, sufficient to localize an initial estimate for a connecting orbit if the two mapped observation manifolds have regions of nonzero intersection. If the submanifolds are mapped into a Hamiltonian canonical set of elements, such as the Delaunay or Hamiltonian elements, the projection of this submanifold into the conjugate pairs of coordinates and momenta must sum to a constant, due to the integral invariants of Poincarè–Cartan. This provides additional structure to these regions as this integral invariance is conserved when mapping in time and thus the area of these projections remains constant.

I. Introduction

A PROBLEM of recent interest to space-faring nations is the tracking, orbit determination, and cataloging of all pieces of artificial space debris particles in low, medium, and high Earth orbits, a population of more than 300,000 particles with diameter larger than 1 cm. The U.S. Air Force Space Command has installed a network of 25 radar and optical sensors for this task, which make about 80,000 observations daily. For more background on observation of space debris, see Rossi [1,2].

Using optical measurements for particles in medium to high Earth orbits, the angles and angular rates of the passing particles, as seen from an Earth-based telescope, can be measured to high precision; however, the range and range rates are largely undetermined. The set of angles and angular rates of such a measurement is called an *attributable vector*. Recent work has been done in outlining a precise mathematical description of the *admissible region* of the range, range-rate plane given an attributable vector observed by radar or optical measurements, Tommei et al. [3]. The admissible region is a two-dimensional surface that lives in the six-dimensional phase space surrounding the Earth. This surface consists of all points in phase space where the true particle can possibly be found. For this reason we will sometimes refer to it as the uncertainty surface. This uncertainty surface is then discretized by a number of points called *virtual debris particles*, or VD particles. Each VD particle is an approximation to a possible orbit for the observed particle of space debris. Viewed as a whole, the set of VD particles forms a *virtual debris field*, or VD field, which approximates the macroscopic uncertainty distribution associated with a given attributable vector. For optical measurements, the admissible region on the range range-rate plane is restricted only by the fact that the debris particle should be gravitationally bound to the Earth (negative geocentric energy) and that it lies within some region (2 and 20 Earth radii) of the observer (Tommei et al. [3]). An extensive study of admissible regions related to the asteroid tracking problem has been done by Milani et al. in [4]. Our preliminary numerical analysis of a randomly chosen attributable vector and its corresponding VD field showed that before several hours had passed, about half of the VDs will have crashed into the Earth. Motivated by these observations, we present in this paper a tighter restriction on the uncertainty region of the range range-rate plane. In particular, in addition to demanding the distance between the debris particle and observer lies between 2 and 20 Earth radii *at the moment of observation*, we place additional restrictions on the periapsis and apoapsis of the orbit. In particular, we require the orbit's periapsis to be greater than 1 Earth radius plus 200 km, and the apoapsis to be less than 25 Earth radii. This places additional constraints on the admissible region and reduces its size considerably. Tommei et al. [3] also proposed a similar, less restrictive addition to the set of constraints defining the admissible region; namely, a lower bound on the semimajor axis.

In Sec. III, we introduce Delaunay variables and discuss the transformation between the observation space (topocentric polar coordinates) and Delaunay space, and the corresponding Jacobian matrix of the transformation. Delaunay variables were introduced by Delaunay [5,6] and can be derived in several ways. One can derive them by solving the Hamilton–Jacobi equations (Born [7]) or by using Lagrange brackets (Abraham and Marsden [8], Brouwer and

Presented as Paper 392 at the AAS/AIAA Astrodynamics Specialist Conference, Mackinac Island, Michigan, 19–23 August 2007; received 29 December 2007; revision received 8 August 2008; accepted for publication 14 August 2008. Copyright © 2008 by Jared M. Maruskin. Published by the American Institute of Aeronautics and Astronautics, Inc., with permission. Copies of this paper may be made for personal or internal use, on condition that the copier pay the $10.00 per-copy fee to the Copyright Clearance Center, Inc., 222 Rosewood Drive, Danvers, MA 01923; include the code 0731-5090/09 $10.00 in correspondence with the CCC.

*Assistant Professor, Department of Mathematics; maruskin@math.sjsu.edu.
†A. Richard Seebass Chair Professor, Department of Aerospace Engineering Sciences; scheeres@colorado.edu.
‡TEES Distinguished Research Chair Professor, Department of Aerospace Engineering; alfriend@aeromail.tamu.edu.

Clemence [9]). A modern geometric derivation is given by Chang and Marsden in [10]. A nice aspect of Delaunay variables is that they can be written in symplectic (canonical) coordinate–conjugate momentum pairs. The corresponding equations of motion, even for the perturbed problem, can be written in the form of Hamilton's equations. Therefore, the integral invariants of Poincaré–Cartan apply, and the sum of the signed area projections onto the three symplectic planes must be conserved. The Delaunay variables are also the action–angle variables of the two body problem; the angles are the coordinates and the actions are the momenta. For the Kepler problem, all Delaunay variables except a single angle variable are conserved. Even though the two-dimensional uncertainty distribution in geocentric Cartesian wraps around the Earth in phase space rapidly, the projection of the same uncertainty distribution on two of the three Delaunay planes is static. The angle variable of the third plane is the mean anomaly, and so all the VD particles march at different rates (which depend only on the mean anomaly's conjugate momentum) along this direction. Because the angle variables are mod2π, the surface begins to wrap around and becomes more and more "shredded" as time progresses. Even in the averaged perturbed problem, only the angle variables change in time, so that the same shredding can be seen in each of the symplectic planes.

In Secs. V, VI, and VII we discuss an algorithm for correlating two observations of the same debris particle. We first consider the case of having two zenith observations at our disposal. We will then add some fuzz to the uncertainty distribution by considering near-zenith observations. Finally we discuss the case when the J_2 term is added to Earth's potential energy. An earlier version of this paper was given by Maruskin et al. [11]. This paper is updated with a more in-depth discussion of the information content in a single track of optical data and in a discussion of the effect of uncertainty in the attributable vector on the distribution in the Delaunay planes.

II. Admissible Region

In this section we shall review the admissible region for a space debris particle observed by a ground based optical sensor, as presented by Tommei et al. [3], and offer an additional physical constraint that will further limit the size of this region in the range range-rate plane.

A. Attributable Vectors

Let $\mathbf{r}$ be the geocentric position of a space debris particle and $\mathbf{r}_O$ the geocentric position of the optical observer. Let the position of the debris particle with respect to the observer be denoted $\mathbf{r}_D = \rho\hat{R}$, where $\hat{R}$ is a unit vector pointing from the observer to the particle. This gives us

$$\mathbf{r} = \mathbf{r}_O + \mathbf{r}_D$$

as shown in Fig. 1. Let

$$(\rho, \alpha, \delta) \in \mathbb{R}^+ \times [-\pi, \pi) \times (-\pi/2, \pi/2)$$

be the spherical polar coordinates defining $\mathbf{r}_D$. Typically one can choose the J2000 coordinate systems so that α is the right ascension and δ is the declination.

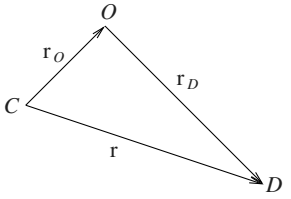

Fig. 1 The space debris particle *D* is observed by the point *O* on the surface of the Earth. The center of the Earth is *C*.

Definition 1: An optical attributable vector is a vector

$$A = (\alpha, \delta, \dot{\alpha}, \dot{\delta}) \in [-\pi, \pi) \times (-\pi/2, \pi/2) \times \mathbb{R}^2$$

observed at time t.

The optical attributable vector is precisely the set of coordinates that can be measured from the observer's frame *on the Earth's surface* at time t. Note that unless the debris particle is seen directly overhead, what we call a zenith measurement, this will translate into uncertainty in the polar angles of the *geocentric* frame. Because the coordinate transformation to the inertial geocentric frame depends on the position of the Earth, additional information must be stored along with the attributable vector. The full set of data that should be tabulated with each observation is

$$x = (A, t, L) \in \mathbb{R}^5 \times \mathbb{N}$$

where $A = (\alpha, \delta, \dot{\alpha}, \dot{\delta})$ is the attributable vector, t is the time of observation, and L is the observatory that made the observation (each observatory can be given integer-valued names). A function can then be defined as follows:

$$\psi\colon (t, L) \to (h, \Theta, \Phi)$$

where h is the altitude of the observatory (which we ignore in the current discussion), and (Θ, Φ) is the inertial angular location of observatory L at time t. The observation data x and inertial orientation function of the observatory ψ can then be unraveled to form the actual usable information for the coordinate transformations

$$\mathcal{X} = (A, t, h, \Theta, \Phi) \in \mathbb{R}^8$$

For simplicity we will take $h = 0$ for the examples worked out in this paper.

B. Measuring Attributable Vectors

One of the primary technical difficulties in space situational awareness (SSA) is the inability to accurately estimate the full dynamical state of an object based on a single track of data. The usual standard for optical only orbit determination is Gauss's method, which requires three measurements of two angles that are sufficiently spread over time and allows one to make a complete orbit determination. In the space debris tracking problem, however, optical search and survey telescopes will observe objects for only very short durations (minutes at most) (Seitzer et al. [12]). This track of data contains information on the angular location of the satellite, but in general does not have sufficient information to allow for an accurate orbit determination of the object (e.g., using Gauss's method). For meaningful orbit characterization, the object must be observed again during a later pass. The problem, of course, is to discern which uncorrelated tracks are the same object.

Our approach to this problem is twofold. First, as described in this section, is to extract the maximum amount of usable information from a single track of a space object and to also bound the possible domain of the unmeasured state components. Second, described in the next section, is to use this information to correlate one observation track with another from a previous observation to detect whether the two objects are the same. In the following we will focus specifically on optical observations of space debris, although the theory and analysis will also apply to radar observations of space debris. This focus is done solely for simplicity of presentation.

The challenge is to extract the maximum amount of usable information from a single track and also derive meaningful constraints on the remaining uncertainty aspects of the state. Instead of determining an overall covariance matrix for the object's state, based on a single track that contains all six dimensions, our approach is to use the track observations to isolate those components of the object's state that can be constrained. For an optical track consisting of several angular observations over a time span of minutes, these are the angular location and angular rate of the object at a specific epoch, generally chosen to lie within the track. The idea is to use the multiple angular measurements to develop an improved estimate of the

angular location of the object and the angular rate of the object, and then use these measurements to constrain the unmeasured states of the object. This approach was recently proposed in [3] by Tommei et al. and is further extended in our research. This approach was also discussed by Milani and Knežević [13] in the context of computing attributable vectors for asteroids from too short of arcs.

If, during an observation period, a space object passes through the field of view of an optical telescope, the optical telescope can take several measurements of that object, equivalent to a series of angles at specific times, with the total time span being a number of minutes. We assume that these angles can be identified with each other to produce a single track of observable data for the space object. There is obviously more information in this pass of data than just a single fix of the angular location of the space object relative to the observer; however, there is not enough information to provide an accurate orbit. To capture this additional information, we can estimate the space object's angular location, angular rate, and angular acceleration at a fixed epoch, chosen within the tracking pass. The additional information content goes into reducing the uncertainty of the angle, angle rate, and angle-acceleration measurement at epoch. This approach recognizes that there is little information in one track related to the object range and range rate, and concentrates on fixing the angles, angle rates, and angle accelerations to a higher level of precision. A similar approach has been taken to estimate the information content of a single pass of Doppler data for an interplanetary spacecraft [14].

The proposed approach is to model the kinematics of the angles; however, it should be noted that the acceleration of either angle is a function of the angles, angle rates, range, and range rate through the equations of motion. Thus, technically, once the angular accelerations and the angle rates are measured for both angles we have an algebraic relationship:

$$\ddot{\alpha} = f_{\alpha}(\alpha, \dot{\alpha}, \delta, \dot{\delta}, \rho, \dot{\rho}) \tag{1}$$

$$\ddot{\delta} = f_{\delta}(\alpha, \dot{\alpha}, \delta, \dot{\delta}, \rho, \dot{\rho}) \tag{2}$$

from which the range and range rate can be solved. Practically, however, there is a large uncertainty in these accelerations which translates to a large uncertainty in the estimated values of ρ and $\dot{\rho}$. From a different perspective, the range and range rate are not being directly measured and can at best be constrained with this approach. Because of these uncertainties we have devised an algorithm which does not rely on estimates of range and range rate to perform initial orbit determination.

In the following we provide an example of this approach for estimating a single angle and its associated rates. This can easily be expanded to a full estimate of both angles. At the heart of the approach is an estimate of the kinematics of the angular motion of the object, in the Earth fixed frame, during the tracking pass. For simplicity in this example we assume the angular motion can be modeled kinematically as

$$\alpha(t) = \alpha_o + \dot{\alpha}_o(t - t_o) + \tfrac{1}{2}\ddot{\alpha}_o(t - t_o)^2 \tag{3}$$

For a general application of this approach, higher order derivatives can be added and estimated and biases in the angular motion can also be added. The biases can be estimated only if tracks are compared between different objects. The problem then reduces to estimating the angular position, angular rate, and angular acceleration of the object at time t_o. For simplicity in this example we assume one-dimensional angular motion and a sequence of N equally spaced observations with uncorrelated error statistics centered on the epoch t_o and covering a time span T. This defines an estimation problem for the angle at epoch α_o, the angular rate at epoch $\dot{\alpha}_o$, and the angular acceleration at epoch $\ddot{\alpha}_o$. There is sufficient information to estimate these provided there are at least three angle measurements in the track.

For simplicity we assume that the individual angle measurements are uncorrelated with each other. Then the least-squares estimation problem is to minimize the cost function

$$J = \frac{1}{2\sigma_{\alpha}^2}\sum_{i=1}^{N}[\alpha(t_i) - \alpha_i]^2 \tag{4}$$

where σ_{α} is the measurement uncertainty, α_i are the actual measurements, and $\alpha(t_i)$ are the predicted measurements. The quantities to estimate are α_o, $\dot{\alpha}_o$, and $\ddot{\alpha}_o$. Forming the necessary equations, and using the fact that $\alpha(t)$ is linear in the quantities to estimate, we form the normal equations:

$$\Lambda \begin{bmatrix} \alpha_o \\ \dot{\alpha}_o \\ \ddot{\alpha}_o \end{bmatrix} = d \tag{5}$$

$$\Lambda = \sum_{i=1}^{N} \frac{1}{\sigma_{\alpha}^2} \begin{bmatrix} 1 & t_i - t_o & \frac{1}{2}(t_i - t_o)^2 \\ t_i - t_o & (t_i - t_o)^2 & \frac{1}{2}(t_i - t_o)^3 \\ \frac{1}{2}(t_i - t_o)^2 & \frac{1}{2}(t_i - t_o)^3 & \frac{1}{4}(t_i - t_o)^4 \end{bmatrix} \tag{6}$$

$$d = \sum_{i=1}^{N} \frac{\alpha_i}{\sigma_{\alpha}^2} \begin{bmatrix} 1 \\ t_i - t_o \\ \frac{1}{2}(t_i - t_o)^2 \end{bmatrix} \tag{7}$$

To characterize the information content in a single pass of data, we can explicitly compute the information matrix Λ. To do this we assume the measurements are taken at equal times $t_i = t_o + (T/2n)i$, where $i = -n, -(n-1), \ldots, -1, 0, 1, \ldots, n$, forming a total of $N = 2n + 1$ measurements over the time span T. Because of this assumption, the odd terms will all sum to zero:

$$\Lambda = (2n+1) \begin{bmatrix} 1 & 0 & \frac{n(n+1)}{6}(\frac{T}{2n})^2 \\ 0 & \frac{n(n+1)}{3}(\frac{T}{2n})^2 & 0 \\ \frac{n(n+1)}{6}(\frac{T}{2n})^2 & 0 & \frac{n(n+1)(3n^2+3n-1)}{60}(\frac{T}{2n})^4 \end{bmatrix} \tag{8}$$

The inverse of this is the covariance matrix $P = \Lambda^{-1}$ that has information on the accuracy to which the angle quantities are measured. To simplify the computation, assume that $n \gg 1$ (often not a valid assumption) and invert the matrix to find

$$P = \frac{\sigma_{\alpha}^2}{(2n+1)} \begin{bmatrix} \frac{9}{4} & 0 & -\frac{15}{2}(\frac{2}{T})^2 \\ 0 & 3(\frac{2}{T})^2 & 0 \\ -\frac{15}{2}(\frac{2}{T})^2 & 0 & 45(\frac{2}{T})^4 \end{bmatrix} \tag{9}$$

with the approximate determinations of

$$\sigma_{\alpha_o} \sim \frac{3\sigma_{\alpha}}{2\sqrt{N}} \tag{10}$$

$$\sigma_{\dot{\alpha}_o} \sim \frac{2\sqrt{3}\sigma_{\alpha}}{T\sqrt{N}} \tag{11}$$

$$\sigma_{\ddot{\alpha}_o} \sim \frac{12\sqrt{5}\sigma_{\alpha}}{T^2\sqrt{N}} \tag{12}$$

and a correlation between the angle and angular acceleration uncertainties. Now consider some published tracking data characteristics for the Michigan Orbital Debris Survey Telescope space surveillance telescope which tracks geosynchronous Earth orbit objects [12]. A usual pass lasts for 5 min during which they take $N = 8$ observations. Several published reports indicate optical sensors have 1 arcsecond or 2.8×10^{-4} deg observation uncertainties, which we use for σ_{α}. This implies that such a track of observations contains information on the angular location and angular rate of the object at epoch t_o with errors on the order of $\sigma_{\alpha_o} \sim 1.5 \times 10^{-4}$ deg, $\sigma_{\dot{\alpha}_o} \sim 1 \times 10^{-6}$ deg/s, and $\sigma_{\ddot{\alpha}_o} \sim 3 \times 10^{-8}$ deg/s^2.

This approach combines the information from a track of observations spread out in time and transforms it into a precise estimate of the partial state of the object at a specific epoch. This is a more convenient form in which to transform the information from the track and makes it easier to discuss constraints on the unmeasured components of the space object's state. For an optical observation these unmeasured components are the object's range and range rate at the epoch t_o.

C. Admissible Region

The specific geocentric energy of the particle is

$$E = \frac{1}{2}\|\dot{\mathbf{r}}\|^2 - \frac{\mu}{\|\mathbf{r}\|}$$

where $\mu = GM_\oplus$ is the gravitational parameter of the Earth. We take $G = 19.91\ \mathrm{R}_\oplus^3\mathrm{M}_\oplus^{-1}\ \mathrm{hr}^{-2}$, where $1\ \mathrm{R}_\oplus = 1$ Earth radius and $1\ \mathrm{M}_\oplus = 1$ Earth mass.

Given an optical attributable vector A, its corresponding admissible region is the set of points on the $(\rho, \dot{\rho})$ plane that have not been ruled out by physical considerations. We impose the following physical constraints on the possible positions of the particle in the topocentric range/range-rate $(\rho, \dot{\rho})$ plane:

1) $\mathcal{C}_1 = \{(\rho, \dot{\rho}) : E < 0\ \mathrm{R}_\oplus^2\ \mathrm{hr}^{-2}\}$
2) $\mathcal{C}_2 = \{(\rho, \dot{\rho}) : 2\ \mathrm{R}_\oplus < \rho < 20\ \mathrm{R}_\oplus\}$
3) $\mathcal{C}_3 = \{(\rho, \dot{\rho}) : 1.03\ \mathrm{R}_\oplus < r_p\}$
4) $\mathcal{C}_4 = \{(\rho, \dot{\rho}) : r_a < 25\ \mathrm{R}_\oplus\}$,

where r_p and r_a are the periapsis and apoapsis (geocentric) radii of the orbit, respectively, and where distance is measured in units of Earth radii. These constraints are introduced by Tommei et al. in [3], though the majority of their work concentrates on analytical aspects of the first two constraints, $\mathcal{C}_1$ and $\mathcal{C}_2$. The latter conditions $\mathcal{C}_3$ and $\mathcal{C}_4$ constrain the periapsis and apoapsis (geocentric) radii of the orbit to always lie within some range. These latter constraints place a restriction on the possible eccentricities of the orbit, which rule out impact orbits and orbits with an extremely high apoapsis. A periapsis of $1.03\ \mathrm{R}_\oplus$ corresponds to a periapsis radius at about 200 km above the surface of the Earth. The admissible region is then defined as a subset of the topocentric range/range-rate plane by the condition:

$$\mathcal{C} = \bigcap_{i=1}^{4} \mathcal{C}_i \tag{13}$$

Given an optical attributable vector A, each point in the $(\rho, \dot{\rho})$ plane corresponds to a unique physical orbit in space that can be determined by a set of geometric and orbital element relations. We start by computing the vectors

$$\hat{R} = \langle \cos\alpha\cos\delta, \sin\alpha\cos\delta, \sin\delta \rangle, \qquad \hat{R}_\alpha := \frac{\partial \hat{R}}{\partial \alpha}, \qquad \hat{R}_\delta := \frac{\partial \hat{R}}{\partial \delta}$$

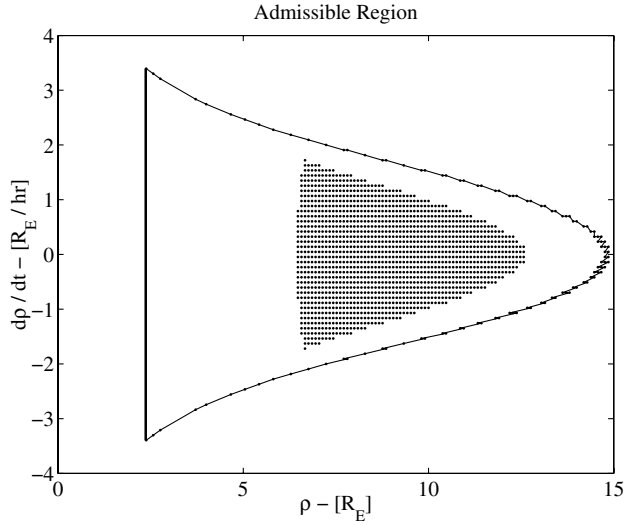

Fig. 2 Admissible region for attributable vector $A = (0, \pi/6, 0.1, 0.03)$, zenith measurement.

The geocentric position and velocity of the particle at $(\rho, \dot{\rho})$ on the range and range-rate plane with attributable vector A is therefore given by

$$\mathbf{r} = \mathbf{r}_O + \rho\hat{R} \tag{14}$$

$$\dot{\mathbf{r}} = \dot{\mathbf{r}}_O + \dot{\rho}\,\hat{R} + \rho\dot{\alpha}\hat{R}_\alpha + \rho\dot{\delta}\hat{R}_\delta \tag{15}$$

Given the position in inertial space, the orbital elements of that orbit are then given by standard relations. To compute the admissible region, we begin by discretizing the strip given by $\mathcal{C}_2$ for a wide range of range rates (e.g., $-10\ \mathrm{R}_\oplus \le \dot{\rho} \le 10\ \mathrm{R}_\oplus$). For each point in the discretization, we compute the physical orbit corresponding to that point and the energy, periapsis radius, and apoapsis radius of that orbit. If the current point in the $(\rho, \dot{\rho})$ plane satisfies the constraints $\mathcal{C}_1$, $\mathcal{C}_3$, and $\mathcal{C}_4$, it is then stored in a separate list that generates the virtual debris field. This second list is a discretization of the admissible region.

Figure 2 shows the admissible region for a given optical observation. In this example, the optical observer's position in standard coordinates is polar angle $\Theta = \pi/3$ rad (measured as the polar angle from the north pole) and azimuthal angle $\Phi = 0$ (measured from the inertial x axis), and the observer makes the following zenith observation $A = (0\ \mathrm{rad}, \pi/6\ \mathrm{rad}, 0.1\ \mathrm{rad/h}, 0.03\ \mathrm{rad/h})$. The outlined region in Fig. 2 is what the admissible region would look like if one chose only to incorporate the constraints $\mathcal{C}_1 \cap \mathcal{C}_2$ (as primarily discussed in [3]). The inside dotted region is the (discretized) admissible region when all four constraints

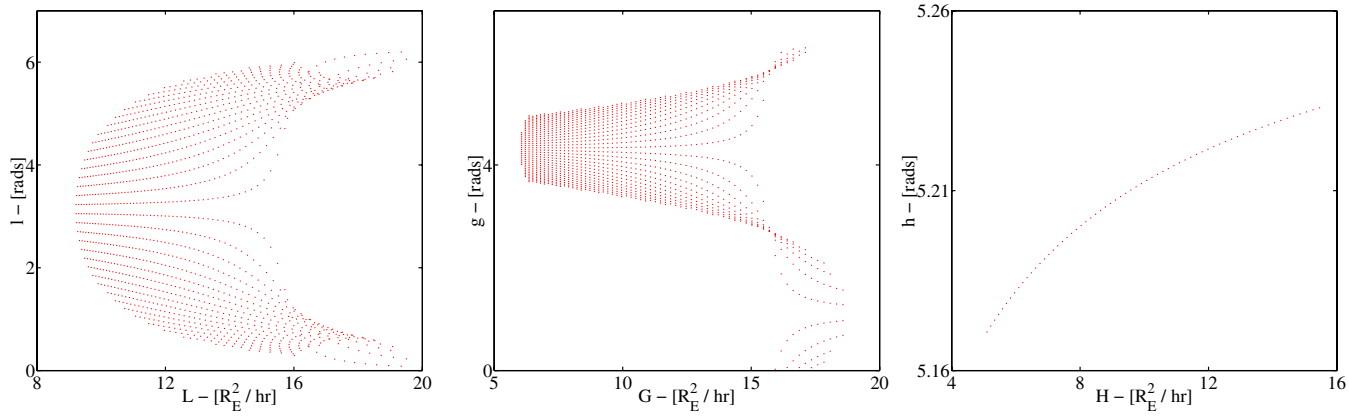

Fig. 3 $T(0;0)\{\mathcal{A}\}$ projected onto the Delaunay planes.

are considered, that is, $\mathcal{C} = \mathcal{C}_1 \cap \mathcal{C}_2 \cap \mathcal{C}_3 \cap \mathcal{C}_4$. As one can see, these additional constraints significantly reduce the area of the admissible region that one must consider in making the orbit determination.

III. Delaunay Variables

In this section, we define the set of canonical Delaunay variables that we use and then indicate how one would compute the corresponding Jacobian matrix of the transformation.

A. Transformation to Delaunay Variables

One can transfer the uncertainty surface (admissible region) into geocentric Cartesian coordinates and then let each point of this surface evolve as a Keplerian orbit. If one does so, one sees that the surface spreads out fairly quickly. As an alternative, we will transfer the surface into Delaunay variables. This is done in several steps. We first transfer the topocentric spherical observation coordinates into geocentric Cartesian coordinates using Eqs. (14) and (15):

$$T_1\colon \langle \rho, \dot{\rho}, \mathfrak{X} \rangle \to \langle x, y, z, \dot{x}, \dot{y}, \dot{z} \rangle$$

This transformation depends on the full set of recorded data $\mathfrak{X} = (A, t, h, \Theta, \Phi)$, as it depends on the location of the observer at that time. As usual, $A = \langle \alpha, \delta, \dot{\alpha}, \dot{\delta} \rangle$ is the admissible vector associated with a given track of data. Next, we transfer the Cartesian coordinates into a set of orbital elements, using standard relations (see Crassidis and Junkins [15], Danby [16], Montenbruck and Gill [17], Roy [18], etc.):

$$T_2\colon \langle x, y, z, \dot{x}, \dot{y}, \dot{z} \rangle \to \langle a, e, i, \omega, \Omega, M \rangle$$

where a is the semimajor axis, e is the eccentricity, i is the inclination, ω is the argument of periapsis, Ω is the longitude of the ascending node, and M is the mean anomaly. Last we transfer the orbital elements into Delaunay variables,

$$T_3\colon \langle a, e, i, \omega, \Omega, M \rangle \to \langle L, l, G, g, H, h \rangle$$

where the Delaunay variables are defined as in Ferraz-Mello [19]:

$$\begin{aligned} l &= M, & L &= \sqrt{\mu a} \\ g &= \omega, & G &= L\sqrt{1-e^2} \\ h &= \Omega, & H &= G\cos i \end{aligned} \tag{16}$$

so that the total transformation from the observation space to Delaunay space at the initial time t_0 is given by the composition:

$$T(t_0; t_0) = T_3 \circ T_2 \circ T_1 \tag{17}$$

The reason for this seemingly superfluous notation, that is, $T(t_0; t_0)$, will be made clear by the end of the section. For the case of zero eccentricity or zero-inclination orbits, the Delaunay variables become singular, and one could instead choose Poincaré nonsingular canonical variables,

$$T_3'\colon \langle a, e, i, \omega, \Omega, M \rangle \to \langle \mathfrak{l}, \mathfrak{L}, \mathfrak{g}, \mathfrak{G}, \mathfrak{h}, \mathfrak{H} \rangle$$

which are defined by the relations:

$$\begin{aligned} \mathfrak{l} &= M + \omega + \Omega, & \mathfrak{L} &= L = \sqrt{\mu a} \\ \mathfrak{g} &= \omega + \Omega & \mathfrak{G} &= G - L = L(\sqrt{1-e^2} - 1) \\ \mathfrak{h} &= \Omega & \mathfrak{H} &= H - G = G(\cos i - 1) \end{aligned}$$

Both the Delaunay variables and the Poincaré nonsingular variables are symplectic sets of coordinate-momenta pairs. The transformations $T_3 \circ T_2$ and $T_3' \circ T_2$ are therefore symplectomorphisms. In this work we will restrict our attention to cases where singularities are not present and one can use Delaunay variables.

We choose Delaunay variables because, similar to the orbital elements, five of them are constants of motion for the unperturbed Kepler problem. Additionally, unlike the orbital elements, there is a natural pairing of the Delaunay variables into coordinate-momenta symplectic pairs, that is, the Delaunay variables l, g, and h are angle variables, to be modded by 2π, and L, G, and H are action variables, or the conjugate momenta. In terms of the Delaunay variables, the equations of motion of the system reduce to Hamilton's equations:

$$\begin{aligned} \frac{\mathrm{d}l}{\mathrm{d}t} &= \frac{\partial \mathcal{F}}{\partial L} & \frac{\mathrm{d}L}{\mathrm{d}t} &= -\frac{\partial \mathcal{F}}{\partial l}\frac{dg}{dt} = \frac{\partial \mathcal{F}}{\partial G} & \frac{\mathrm{d}G}{\mathrm{d}t} &= -\frac{\partial \mathcal{F}}{\partial g} \\ \frac{\mathrm{d}h}{\mathrm{d}t} &= \frac{\partial \mathcal{F}}{\partial H} & \frac{\mathrm{d}H}{\mathrm{d}t} &= -\frac{\partial \mathcal{F}}{\partial h} \end{aligned} \tag{18}$$

where

$$\mathcal{F} = -\frac{\mu^2}{2L^2} + \mathcal{R}(L, l, G, g, H, h)$$

and where $\mathcal{R}(L, l, G, g, H, h)$ is the disturbing force expressed in terms of Delaunay variables. For the unperturbed Kepler problem, the equations of motion work out as

$$\frac{\mathrm{d}l}{\mathrm{d}t} = \frac{\mu^2}{L^3}, \qquad \frac{\mathrm{d}L}{\mathrm{d}t} = \frac{\mathrm{d}H}{\mathrm{d}t} = \frac{\mathrm{d}G}{\mathrm{d}t} = \frac{\mathrm{d}h}{\mathrm{d}t} = \frac{\mathrm{d}g}{\mathrm{d}t} = 0 \tag{19}$$

For the general case, we can denote the Hamiltonian flow of Eq. (18) as

$$\begin{aligned} T_4(t; t_0)\colon & \langle L(t_0), l(t_0), G(t_0), g(t_0), H(t_0), h(t_0) \rangle \\ & \to \langle L(t), l(t), G(t), g(t), H(t), h(t) \rangle \end{aligned}$$

For the Kepler problem, this simplifes to the form:

$$\begin{aligned} & T_4^{\text{Kepler}}(t; t_0)(L_0, l_0, G_0, g_0, H_0, h_0) \\ & \quad = \left\langle L_0, \left(l_0 + \frac{\mu^2}{L_0^3}(t - t_0) \right), G_0, g_0, H_0, h_0 \right\rangle \end{aligned}$$

The transformation from the observation space to the time-evolved Delaunay space is then given by

$$T(t; t_0) = T_4(t; t_0) \circ T(t_0; t_0) \tag{20}$$

where $T(t_0; t_0)$ is defined in Eq. (17). This is well defined because $T_4(t_0; t_0)$ is the identity transformation.

B. Jacobian Matrix

As we shall see, the Jacobian matrix of the transformation T will be used to compute variations in the Delaunay variables with respect to variations in the $(\rho, \dot{\rho})$ plane. Because the variables $(\alpha, \dot{\alpha}, \delta, \dot{\delta})$ are taken to be known, we need only consider the first two columns of the Jacobian of T. We will denote this 6×2 matrix as Φ. We construct Φ by composition. First we define

$$\begin{aligned} \Phi_1 &= \frac{\partial(x, y, z, \dot{x}, \dot{y}, \dot{z})}{\partial(\rho, \dot{\rho})} \\ &= \begin{bmatrix} \cos\alpha\cos\delta & 0 \\ \sin\alpha\cos\delta & 0 \\ \sin\delta & 0 \\ -\dot{\alpha}\sin\alpha\cos\delta - \dot{\delta}\cos\alpha\sin\delta & \cos\alpha\cos\delta \\ \dot{\alpha}\cos\alpha\cos\delta - \dot{\delta}\sin\alpha\sin\delta & \sin\alpha\cos\delta \\ \dot{\delta}\cos\delta & \sin\delta \end{bmatrix} \end{aligned}$$

where the partial derivatives have been computed using the transformation relations (14) and (15).

Next, the Jacobian of the transformation T_2 is computed

$$\Phi_2 = \frac{\partial(a, e, i, \omega, \Omega, M)}{\partial(x, y, z, \dot{x}, \dot{y}, \dot{z})}$$

A very efficient and elegant algorithm to compute this matrix is given in [20] by Montenbruck and Gill.

The Jacobian of the transformation matrix T_3 is then computed

$$\Phi_3 = \frac{\partial(L,l,G,g,H,h)}{\partial(a,e,i,\omega,\Omega,M)} = \begin{bmatrix} L_a & 0 & 0 & 0 & 0 & 0 \\ 0 & 0 & 0 & 0 & 0 & 1 \\ L_a\sqrt{1-e^2} & G_e & 0 & 0 & 0 & 0 \\ 0 & 0 & 0 & 1 & 0 & 0 \\ L_a\sqrt{1-e^2}\cos i & G_e\cos i & -G\sin i & 0 & 0 & 0 \\ 0 & 0 & 0 & 0 & 1 & 0 \end{bmatrix}$$

where

$$L_a = \frac{1}{2}\sqrt{\frac{\mu}{a}} \quad \text{and} \quad G_e = \frac{-Le}{\sqrt{1-e^2}}$$

Finally, the Jacobian corresponding to the time evolution of the system (18) can be found using standard techniques (see Maruskin et al. [21] for the procedure):

$$\Phi_4(t;t_0) = \frac{\partial(L(t),l(t),G(t),g(t),H(t),h(t))}{\partial(L(t_0),l(t_0),G(t_0),g(t_0),H(t_0),h(t_0))}$$

This Jacobian matrix, because it corresponds to a time evolution transformation, is also known as the state transition matrix (STM) of the evolution map. For the Kepler case, this STM takes the simple analytic form:

$$\Phi_4^{\text{Kepler}}(t;t_0) = \begin{bmatrix} 1 & 0 & 0 & 0 & 0 & 0 \\ -3\mu^2(t-t_0)/L_0^4 & 1 & 0 & 0 & 0 & 0 \\ 0 & 0 & 1 & 0 & 0 & 0 \\ 0 & 0 & 0 & 1 & 0 & 0 \\ 0 & 0 & 0 & 0 & 1 & 0 \\ 0 & 0 & 0 & 0 & 0 & 1 \end{bmatrix} \tag{21}$$

The 6×2 matrix Φ, which is the first two columns of the Jacobian of T, is then given by

$$\Phi(t;t_0) = \Phi_4(t;t_0)\cdot\Phi_3\cdot\Phi_2\cdot\Phi_1$$

and it maps a variation in the admissible region to a variation in the Delaunay variables, that is,

$$\begin{bmatrix} \delta L \\ \delta l \\ \delta G \\ \delta g \\ \delta H \\ \delta h \end{bmatrix} = \Phi_{6\times 2}\cdot\begin{bmatrix} \delta\rho \\ \delta\dot{\rho} \end{bmatrix}$$

Additionally, the following three 2×2 symplectic submatrices of $\Phi(t;t_0)$ will be considered:

$$\mathbb{L}(t;t_0) = [I_2 \quad 0_2 \quad 0_2]\cdot\Phi(t;t_0)$$
$$\mathbb{G}(t;t_o) = [0_2 \quad I_2 \quad 0_2]\cdot\Phi(t;t_0)$$
$$\mathbb{H}(t;t_0) = [0_2 \quad 0_2 \quad I_2]\cdot\Phi(t;t_0)$$

where 0_2 and I_2 are the 2×2 matrix of zeros and identity matrix, respectively. These are defined so that

$$\begin{bmatrix} \delta L \\ \delta l \end{bmatrix} = \mathbb{L}\cdot\begin{bmatrix} \delta\rho \\ \delta\dot{\rho} \end{bmatrix}$$
$$\begin{bmatrix} \delta G \\ \delta g \end{bmatrix} = \mathbb{G}\cdot\begin{bmatrix} \delta\rho \\ \delta\dot{\rho} \end{bmatrix}, \quad \text{and} \quad \begin{bmatrix} \delta H \\ \delta h \end{bmatrix} = \mathbb{H}\cdot\begin{bmatrix} \delta\rho \\ \delta\dot{\rho} \end{bmatrix}$$

Notice that, because of the especially simple form $\Phi_4(t;t_0)$ takes in the Kepler case (21), the dynamic time evolution of the system *affects only the submatrix* $\mathbb{L}$ of the full STM $\Phi(t;t_0)$. Thus, once the matrices $\mathbb{G}$ and $\mathbb{H}$ are computed for a VD particle, they are constant in time. Note that they still depend on the VD particle, as they depend on $\alpha, \dot{\alpha}, \delta, \dot{\delta}, \rho, \dot{\rho}$, the location of the optical observer on Earth, and the time of the measurement (which gives the observer's position in *inertial* space).

IV. Intersection Theory Analysis

In this section we describe how the Delaunay space can be used in fitting an orbit determination between two previously uncorrelated tracks (UCTs). In subsequent sections we will illustrate this technique for a sample set of observations, considering separately zenith and nonzenith observations, and additionally the effect of the J_2 term in Earth's potential on the proposed orbit determination process.

A. Mapping the Admissible Region to Delaunay Space

Let $\mathcal{D} \cong \mathbb{R}^6$ be the six-dimensional Delaunay space and $\mathcal{C}(\mathcal{X})$ the corresponding admissible region in the topocentric range/range-rate plane for a fixed attributable vector and spatiotemporal observation location, as defined in Eq. (13). For a fixed epoch time τ, we define the map $F_{\mathcal{X}}^{\tau}\colon \mathcal{C} \to \mathcal{D}$ as the restriction of the map $T(\tau;t)$ defined in Eq. (20) for a fixed $\mathcal{X}$, where t is the time of the observation (one of the components of $\mathcal{X}$), so that

$$F_{\mathcal{X}}^{\tau}\colon \langle\rho,\dot{\rho}\rangle \to \langle L,l,G,g,H,h\rangle$$

Thus $F_{\mathcal{X}}^{\tau}(\mathcal{C}) \subset \mathcal{D}$ is a two-dimensional submanifold of Delaunay space $\mathcal{D} \cong \mathbb{R}^6$. We further define the three *Delaunay projective spaces* $\mathcal{D}_L \cong \mathcal{D}_G \cong \mathcal{D}_H \cong \mathbb{R}^2$, so that the Delaunay space $\mathcal{D}$ has the direct sum decomposition $\mathcal{D} = \mathcal{D}_L \oplus \mathcal{D}_G \oplus \mathcal{D}_H$. These three projective spaces are the projections of Delaunay space onto the three symplectic Delaunay planes. If Π_L, Π_G, and Π_H are the projection operators from the full six-dimensional Delaunay space onto the symplectic Delaunay planes, so that $\Pi_L(L,l,G,g,H,h) = \langle L,l\rangle$, etc., then $\mathcal{D}_L = \Pi_L(\mathcal{D})$, $\mathcal{D}_G = \Pi_G(\mathcal{D})$, and $\mathcal{D}_H = \Pi_H(\mathcal{D})$. The map $F_{\mathcal{X}}^{\tau}$ can thus be thought of in either of two ways, as a one-to-one mapping from the two-dimensional admissible region $\mathcal{C}$ to the six-dimensional Delaunay space $\mathcal{D}$ or as a one-to-three mapping from the two-dimensional admissible region $\mathcal{C}$ to the three two-dimensional Delaunay projective spaces $\mathcal{D}_L$, $\mathcal{D}_G$, and $\mathcal{D}_H$. Although at first glance, such a distinction seems pedantic, it is actually an important one, as intersections are inherently easier to both visualize and carry out in two-dimensional spaces then they are in six-dimensional spaces.

B. Necessary Conditions for Correlation Between Two Uncorrelated Tracks

The SSA problem is, in essence, to determine which UCTs of data correspond to the same physical object. Once this is known, a preliminary orbit determination can be made from those two tracks of data and the orbit can be stored in the space debris catalog. In this discussion we discuss how to compare pairwise UCTs to determine whether they correlate to the same object.

Given two extended attributable vectors $\mathcal{X}_1$ and $\mathcal{X}_2$, one determines the corresponding admissible regions $\mathcal{C}_1$ and $\mathcal{C}_2$, respectively. These admissible regions cannot be compared directly, as they are subsets of two different sets of topocentric spherical coordinates, affixed to the Earth at different locations and different times. We now push the admissible regions forward into Delaunay space, and dynamically evolve or regress both uncertainty distributions in time to a common epoch τ, so that $F_{\mathcal{X}_1}^{\tau}(\mathcal{C}_1)$ and $F_{\mathcal{X}_2}^{\tau}(\mathcal{C}_2)$ are both two-dimensional submanifolds of six-dimensional Delaunay space $\mathcal{D}$, dynamically mapped to a common epoch time.

If $\mathcal{X}_1$ and $\mathcal{X}_2$ correspond to the same object, then $F_{\mathcal{X}_1}^{\tau}(\mathcal{C}_1)$ and $F_{\mathcal{X}_2}^{\tau}(\mathcal{C}_2)$ must necessarily intersect. Because $\mathcal{X}_1$ and $\mathcal{X}_2$ each contain four pieces of information (two angles and two angle rates), the system is overdetermined. Unless there is some redundancy in the information, if both tracks correspond to the same physical object, it

is likely that the uncertainty manifolds $F^{\tau}_{\mathfrak{X}_1}(\mathcal{C}_1)$ and $F^{\tau}_{\mathfrak{X}_2}(\mathcal{C}_2)$ will intersect at a single point $\boldsymbol{\Delta}^*$.

On the other hand, suppose that it is still unknown whether both attributable vectors correspond to the same physical object, but the surfaces $F^{\tau}_{\mathfrak{X}_1}(\mathcal{C}_1)$ and $F^{\tau}_{\mathfrak{X}_2}(\mathcal{C}_2)$ are found to intersect at a single point. We can then conclude with a high confidence that both attributable vectors correspond to the same object. The reason is that $F^{\tau}_{\mathfrak{X}_1}(\mathcal{C}_1)$ and $F^{\tau}_{\mathfrak{X}_2}(\mathcal{C}_2)$ are both two-dimensional manifolds embedded into the same six-dimensional Delaunay space $\mathcal{D}$. The probability that they, *by accident*, happen to touch tangentially at a single intersection point $\boldsymbol{\Delta}^*$ is extremely low, unless they are correlated and the orbit for both objects is given by that common intersection point $\boldsymbol{\Delta}^*$. A preliminary orbit determination is then given by the intersection point $\boldsymbol{\Delta}^*$ and the two tracks may be considered to be correlated. One then places this preliminary orbit determination into a separate holding catalog and awaits confirmation by a third consistent track of data, at which time the orbit is added to the standard catalog.

The topic of determining this intersection point is taken up in the next paragraph.

C. Intersection Theory Analysis

Supposing two extended attributable vectors $\mathfrak{X}_1$ and $\mathfrak{X}_2$ correspond to the same physical object, a unique intersection point $\boldsymbol{\Delta}^*$ of the two submanifolds $F^{\tau}_{\mathfrak{X}_1}(\mathcal{C}_1)$ and $F^{\tau}_{\mathfrak{X}_2}(\mathcal{C}_2)$ can be found. To do this, we will consider the threefold projection of these surfaces onto the Delaunay planes. To reduce complexity of notation let us define

$$S^i_L = \Pi_L\left(F^{\tau}_{\mathfrak{X}_i}(\mathcal{C}_i)\right) \subset \mathcal{D}_L \qquad S^i_G = \Pi_G\left(F^{\tau}_{\mathfrak{X}_i}(\mathcal{C}_i)\right) \subset \mathcal{D}_G$$

$$S^i_H = \Pi_H\left(F^{\tau}_{\mathfrak{X}_i}(\mathcal{C}_i)\right) \subset \mathcal{D}_H$$

For each of the symplectic Delaunay surface projections, there is an overlap region

$$S^1_L \cap S^2_L \qquad S^1_G \cap S^2_G \qquad S^1_H \cap S^2_H$$

[See, for example, Fig. 9 (the overlap regions are not highlighted) in Sec. VI.] We know that if the two tracks were of the same object, the true orbit must be in each of these intersected regions, that is, $\Pi_L(\boldsymbol{\Delta}^*) \in S^1_L \cap S^2_L$ and similarly for the G and H projections. However, because each projection is a unique view of the same two two-dimensional surfaces, more information can be extracted. To obtain the unique intersection point, one carries out the following algorithm, which we have named intersection theory analysis (ITA):

1) Select a Delaunay plane $\mathcal{P}$ (so that $\mathcal{P}$ represents either the L, G, or H Delaunay plane).

2) The projection of $\boldsymbol{\Delta}^*$ must lie in the intersection of the two projected uncertainty surfaces, that is, $\boldsymbol{\Delta}^* \in S^1_{\mathcal{P}} \cap S^2_{\mathcal{P}}$. Both projections $S^1_{\mathcal{P}}$ and $S^2_{\mathcal{P}}$ are discretized by a population of VD particles that have been mapped into the Delaunay space. Omit all VD particles that do not lie in the overlap region. Now define

$$\diamond F^{\tau}_{\mathfrak{X}_i}(\mathcal{C}_i) \subset F^{\tau}_{\mathfrak{X}_i}(\mathcal{C}_i) \subset \mathcal{D}$$

by the relation

$$\Pi_{\mathcal{P}}\left(\diamond F^{\tau}_{\mathfrak{X}_i}(\mathcal{C}_i)\right) = S^1_{\mathcal{P}} \cap S^2_{\mathcal{P}}$$

3) Now reproject both surfaces $\diamond F^{\tau}_{\mathfrak{X}_1}(\mathcal{C}_1)$ and $\diamond F^{\tau}_{\mathfrak{X}_2}(\mathcal{C}_2)$ onto the Delaunay planes. Define their projections as

$$\diamond S^i_L = \Pi_L\left(\diamond F^{\tau}_{\mathfrak{X}_i}(\mathcal{C}_i)\right) \subset \mathcal{D}_L \qquad \diamond S^i_G = \Pi_G\left(\diamond F^{\tau}_{\mathfrak{X}_i}(\mathcal{C}_i)\right) \subset \mathcal{D}_G$$

$$\diamond S^i_H = \Pi_H\left(\diamond F^{\tau}_{\mathfrak{X}_i}(\mathcal{C}_i)\right) \subset \mathcal{D}_H$$

(See Fig. 10 for an example of this.) Notice that, in this figure, all nonoverlap points on the Delaunay plane $\mathcal{D}_H$ have been omitted.

4) Repeat steps 1–3. For step 1 choose a different $\mathcal{P}$. It is alright if you have used that $\mathcal{P}$ before, as long as you do not use the same $\mathcal{P}$ twice in a row. For steps 2–3, add an extra diamond to each strand of diamonds to indicate that an additional reduction has taken place. Continue until you are left with a single (approximate) intersection point.

The diamond operator is identified with omitting all nonoverlap regions in a particular Delaunay plane. The process of orbit determination is therefore reduced to the development of an efficient computer algorithm that will determine this overlap region for two overlapping discretized laminas on $\mathbb{R}^2$. This procedure is illustrated over the next several sections of the paper, as an initial feasibility study of the ITA algorithm. For the current work, the overlap regions were computed by manual computation and by trial and error. Creating a computer algorithm that determines these overlap regions automatically will be a focus of future research.

V. Orbit Determination 1: Kepler Orbit with Two Zenith Observations

A. Concurrent Plot of Two Zenith Observations on the Delaunay Planes

In this section we consider the admissible region corresponding to the zenith observation $A = (0\text{ rad}, \pi/6\text{ rad}, 0.1\text{ rad/h}, 0.03\text{ rad/h})$, made at $t = 0$ h from a point on the Earth's surface $\Theta = \pi/3$ rad, $\Phi = 0$ rad. The admissible region of the $(\rho, \dot{\rho})$ plane is the inner discretized region plotted in Fig. 2. Each district of the discretization is referred to as a VD particle. We will think of the uncertainty region as a two-dimensional surface in a six-dimensional space,

$$\mathcal{A} := \{\langle \rho, \dot{\rho}, \alpha, \delta, \dot{\alpha}, \dot{\delta}\rangle : (\alpha, \delta, \dot{\alpha}, \dot{\delta}) = A \text{ and } (\rho, \dot{\rho}) \in \mathcal{C}\}$$

where $\mathcal{C}$ is the admissible region defined in Eq. (13). We call $\mathcal{C}$ the admissible region of the $(\rho, \dot{\rho})$ plane and $\mathcal{A}$ the admissible region of the observation space. Define

$$T_1\{\mathcal{A}\} := \{\langle r, \dot{r}\rangle \in \mathbb{R}^6 : T_1^{-1}(\langle r, \dot{r}\rangle) \in \mathcal{A}\}$$

that is, $T_1\{\mathcal{A}\}$ is the image of $\mathcal{A}$ under the mapping T_1. Then $T_1\{\mathcal{A}\}$ is a two-dimensional surface in the geocentric Cartesian phase space. Similarly, we define

$$T(t; t_0)\{\mathcal{A}\} := \{x = \langle L, l, G, g, H, h\rangle \in \mathbb{R}^6 : T(t; t_0)^{-1} \cdot x \in \mathcal{A}\}$$

where $T(t; t_0)$ is defined by the relations in Sec. III.A. $T(t; t_0)\{\mathcal{A}\}$ is a two-dimensional surface in Delaunay space. Because $T_1\{\mathcal{A}\}$ is allowed to move about relatively freely, fold, wrap around the planet, etc., we will choose to follow the dynamic evolution of the surface $T(t; t_0)\{\mathcal{A}\}$ instead, which has a much more restricted evolution.

The projections of $T(0; 0)\{\mathcal{A}\}$ onto the three symplectic Delaunay planes are shown in Fig. 3. Because the phase flow is Hamiltonian and the Delaunay variables are a set of coordinate-momentum symplectic pairs, the sum of the oriented area projections onto the Delaunay planes is conserved [22]. Because all of the Delaunay variables except for l are constants of motion for the Kepler problem, the total area projection on the $(L - l)$ Delaunay plane will be conserved, unless the surface "folds over," as was discussed by Scheeres et al. in [23]. Because the observation was made directly overhead, a certain degeneracy exists that causes the projection of the uncertainty region on the (H, h) Delaunay plane to be a line, as in Fig. 3.

The dynamics for the Kepler problem, in terms of Delaunay variables, is governed by the equations of motion (19). In particular, $\mathrm{d}l/\mathrm{d}t \propto L^{-3}$. All of the dots in the (L, l) plane will march up the graph. Because the angle l is given mod2π, when a dot reaches $l = 2\pi$, it is reset to $l = 0$. The regions for smaller L will move at a greater constant rate than the regions for larger L. In this way a shearing effect takes place. The dynamics literally shreds the region into thin strips. The longer you wait, the more thin strips the uncertainty region will be cut up into. After 70 h, the surface $T(70; 0)\{\mathcal{A}\}$ is projected onto the symplectic Delaunay planes, and is shown in Fig. 4. Notice the projections onto the (G, g) and (H, h) plane are unchanged.

At time $t = 70$ h we will assume that we have another zenith observation of the same particle of space debris. MATLAB

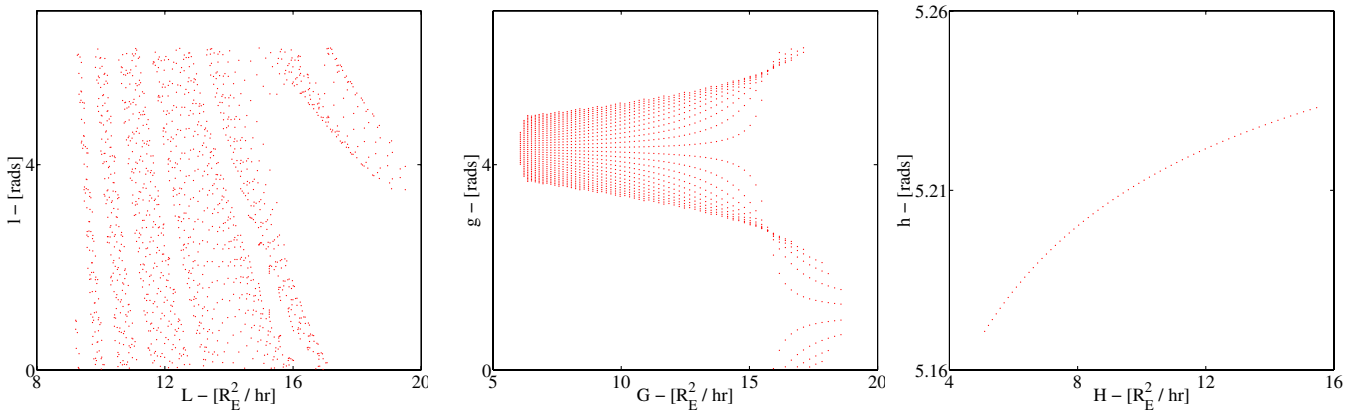

Fig. 4 $T(70;0)\{\mathcal{A}\}$ projected onto the Delaunay planes.

randomly selected VD field particle no. 893 to correspond to the actual physical piece of debris. If VD particle no. 893 were to be observed again at time $t = 70$ h by an Earth bound optical observer with inertial polar angle $\Theta = 1.1650$ rad (measured from the north pole) and azimuthal angle $\Phi = 5.9214$ rad (measured from the inertial x axis), its attributable vector would be $A_{70} = (\alpha, \delta, \dot{\alpha}, \dot{\delta}) = (-0.3618 \text{ rad}, 0.4058 \text{ rad}, 0.0315 \text{ rad/h}, 0.0209 \text{ rad/h})$. Because $\alpha = \Phi - 2\pi$ rad and $\delta = \pi/2 - \Theta$ rad, this is again a zenith observation. For this second observation, $t_0 = 70$ h, and so the initial transformation of the admissible region of the observation space $\mathcal{A}_{70}$ to the Delaunay space would be $T(70;70)\{\mathcal{A}_{70}\}$. $\mathcal{A}_{70}$ is the *new* observation recorded at time $t = 70$. $T(70;0)\{\mathcal{A}\}$ and $T(70;70)\{\mathcal{A}_{70}\}$ are plotted concurrently on each of the Delaunay planes in Fig. 5.

The intersection of the two lines in the $(H - h)$ plane in Fig. 5 indicates that the Delaunay variables H and h can be determined exactly. This reduces the uncertainty region to a one-dimensional uncertainty curve, because each point on each line in the (H, h) plane is a curve in the original $(\rho, \dot{\rho})$ admissible region.

B. Determining the Intersection Point on the $(H - h)$ Plane

As earlier noted, if both observations are zenith observations, the uncertainty region projected onto the $(H - h)$ plane will degenerate to a single line, for both observations. We will therefore begin by determining this intersection point, which will pinpoint the values of H and h that belong to the true debris particle. We will use the Jacobian matrix derived in Sec. III.B as part of a predictor-corrector method in determining this intersection point.

One would have to be fairly lucky to by chance have discretized the initial $(\rho, \dot{\rho})$ plane so that $T(70;0)\{\mathcal{A}\}$ has a point *exactly* on the intersection in the (H, h) plane. If we were to zoom in on the intersection point in Fig. 5, we would be more likely to see something as in Fig. 6. Here the light (red) points are the images of VD particles from the initial observation, projected onto the (H, h) plane, that is, they are points from the set $T(70;0)\{\mathcal{A}\}$. Similarly, the dark (black) points are from the new observation, that is, they are from the set $T(70;70)\{\mathcal{A}_{70}\}$. Because of the degeneracy that exists for zenith observations, the preimage of each point on the (H, h) plane is actually a curve in the initial topocentric admissible region in the $(\rho, \dot{\rho})$ space. Our first goal is to determine *a single point* in each admissible region that maps to the intersection point in the Delaunay projective space $\mathcal{D}_H$. We will show how to use this single point to generate the full curve in the admissible region that projects onto this intersection point in the next section.

For convenience we will use the coordinates $(\rho, \dot{\rho})$ as coordinates for the initial admissible region $\mathcal{C}$ belonging to the first observation and the coordinates $(\varrho, \dot{\varrho})$ as coordinates for the second admissible region $\mathcal{C}_{70}$ belonging to the second observation.

We begin by choosing an initial guess. We take one of the intersection point's neighboring points $\langle H_0, h_0\rangle \in T(70;0)\{\mathcal{A}\}$, which is mapped from $\langle \rho, \dot{\rho}\rangle \in \mathcal{C}$. The partial Jacobian matrix $\mathbb{H}$ tells us the effect of varying $\langle \rho, \dot{\rho}\rangle$ on the point $\langle H, h\rangle$, that is, for the dark (black) points in Fig. 6:

$$\begin{bmatrix} \delta H_0 \\ \delta h_0 \end{bmatrix} = \mathbb{H}_0 \begin{bmatrix} \delta\rho \\ \delta\dot{\rho} \end{bmatrix}$$

Similarly for the second observation, we will consider the nearby point $\langle H_{70}, h_{70}\rangle$ which belongs to the point $\langle \varrho, \dot{\varrho}\rangle$ of the admissible region. Thus, for the light (red) points in Fig. 6:

$$\begin{bmatrix} \delta H_{70} \\ \delta h_{70} \end{bmatrix} = \mathbb{H}_{70} \begin{bmatrix} \delta\varrho \\ \delta\dot{\varrho} \end{bmatrix}$$

So the game now is to find a set of points on both admissible regions, $\langle \delta\rho, \delta\dot{\rho}\rangle$ and $\langle \delta\varrho, \delta\dot{\varrho}\rangle$, so that their images under the mapping $T(70;0)$ and $T(70;70)$, respectively, lie on the intersection point.

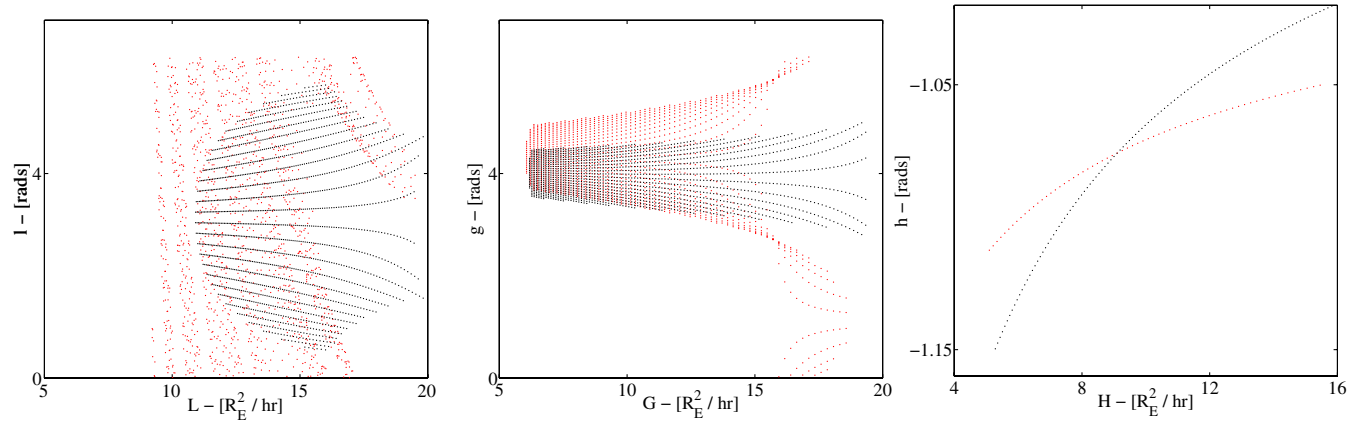

Fig. 5 $T(70;0)\{\mathcal{A}\}$ (light) (red) and $T(70;70)\{\mathcal{A}_{70}\}$ (dark) (black) projected onto the Delaunay planes.

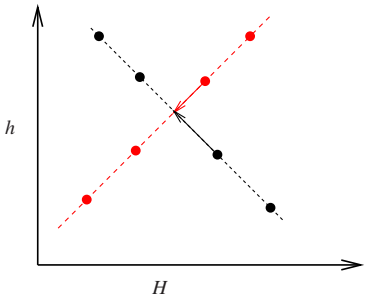

Fig. 6 Example schematic for locating the intersection point on the $(H-h)$ plane.

The condition is

$$\begin{bmatrix} H_{70} \\ h_{70} \end{bmatrix} + \mathbb{H}_{70} \cdot \begin{bmatrix} \delta\varrho \\ \delta\dot{\varrho} \end{bmatrix} = \begin{bmatrix} H_0 \\ h_0 \end{bmatrix} + \mathbb{H}_0 \cdot \begin{bmatrix} \delta\rho \\ \delta\dot{\rho} \end{bmatrix}$$

This can be rearranged as follows:

$$\begin{bmatrix} \Delta H \\ \Delta h \end{bmatrix} := \begin{bmatrix} H_{70} - H_0 \\ h_{70} - h_0 \end{bmatrix} = \mathbb{H}_0 \cdot \begin{bmatrix} \delta\rho \\ \delta\dot{\rho} \end{bmatrix} - \mathbb{H}_{70} \cdot \begin{bmatrix} \delta\varrho \\ \delta\dot{\varrho} \end{bmatrix} \tag{22}$$

Because the image of the admissible region $\mathcal{A}$ under the transformation $T(t;t_0)$ is a line when projected onto the (H,h) plane, both state transition matrices $\mathbb{H}_0$ and $\mathbb{H}_{70}$ have a single zero eigenvector. Because of this degeneracy, there is no one unique predictor vector. However, we are only looking for a single point in the admissible region that corresponds to the intersection point on the (H,h) plane. The easiest approach is to do the following. If $\langle 1,0\rangle^T \notin \text{null}(\mathbb{H}_0)$, we take $\delta\dot{\rho}=0$; otherwise we take $\delta\rho=0$. Additionally, if $\langle 1,0\rangle^T \notin \text{null}(\mathbb{H}_{70})$, we take $\delta\dot{\varrho}=0$; otherwise we take $\delta\varrho=0$. For considerations here, we will assume both $\langle 1,0\rangle^T \notin \text{null}(\mathbb{H}_0)$ and $\langle 1,0\rangle^T \notin \text{null}(\mathbb{H}_{70})$, so that we can take $\delta\dot{\rho}=0$ and $\delta\dot{\varrho}=0$. If either of these conditions fails, the procedure presented here can be easily modified accordingly.

Begin by defining $\mathbf{z} = \langle \Delta H, \Delta h\rangle^T$. Let $\mathbf{h}_0$ and $\mathbf{h}_{70}$ be the first columns of the matrices $\mathbb{H}_0$ and $\mathbb{H}_{70}$, respectively. Let $\mathbf{h}_0^\perp$ and $\mathbf{h}_{70}^\perp$ be unit vectors perpendicular to the vectors $\mathbf{h}_0$ and $\mathbf{h}_{70}$, respectively. Then by prescribing the conditions $\delta\dot{\rho}=0$ and $\delta\dot{\varrho}=0$, Eq. (22) reduces to

$$\mathbf{z} = (\delta\rho)\mathbf{h}_0 - (\delta\varrho)\mathbf{h}_{70}$$

Dotting this equation with $\mathbf{h}_{70}^\perp$ and solving for $\delta\rho$ we obtain

$$\delta\rho = \frac{\mathbf{h}_{70}^\perp \cdot \mathbf{z}}{\mathbf{h}_{70}^\perp \cdot \mathbf{h}_0}$$

Similarly, by dotting with $\mathbf{h}_0^\perp$, we can obtain the following for $\delta\varrho$:

$$\delta\varrho = -\frac{\mathbf{h}_0^\perp \cdot \mathbf{z}}{\mathbf{h}_0^\perp \cdot \mathbf{h}_{70}}$$

This now gives us a new approximation for the intersection point. We reapply as necessary.

Both of the 2×2 $\mathbb{H}$-matrices will have a degeneracy in the form of a zero eigenvalue. The corresponding eigenvector we call the *zero eigenvector*. The zero eigenvector itself is *not* the zero vector, rather it is the eigenvector that corresponds to the zero eigenvalue, that is, the vector whose span is the null space of $\mathbb{H}$. $\mathbb{H}$ clearly has a zero eigenvector, if the initial observation is made at zenith, because the two-dimensional uncertainty region $\mathcal{C}$ on the $(\rho,\dot{\rho})$ plane reduces to a one-dimensional line on the (H,h) plane. Suppose $\xi(\rho,\dot{\rho})$ is the zero eigenvector of $\mathbb{H}$ at $(\rho,\dot{\rho}) \in \mathcal{C}$. The above algorithm provides a single point $(\rho^*,\dot{\rho}^*) \in \mathcal{C}$ that maps to the intersection point on the (H,h) plane. There exists a one-dimensional curve $\gamma(s)$: $(E \subset \mathbb{R}) \to \mathcal{C}$, such that $\gamma(0) = (\rho^*,\dot{\rho}^*)$, $\gamma(s) = (\rho(s),\dot{\rho}(s))$, and such that the projection onto the (H,h) plane of the image of γ under the mapping $T(70;0)$ is the single intersection point of the two admissible curves on the (H,h) plane. The curve γ is then generated by the condition that $\gamma'(s) = \xi(\rho(s),\dot{\rho}(s))$, for all $s \in E$. So to generate a discretized sequence of points along γ, we integrate the zero eigenvector of $\mathbb{H}$, starting from $(\rho^*,\dot{\rho}^*)$, until the curve exits the admissible region $\mathcal{C}$. In this way, once we determine a single point $(\rho^*,\dot{\rho}^*)$ on the admissible region $\mathcal{C}$ that corresponds to the intersection point in (H,h) space, a reduced admissible region $\mathcal{C}^r \subset \mathcal{C}$ can then be defined.

If the observation is made at zenith, we have that $\dot{\rho}=\dot{r}$, that is, the rate of change of the radial coordinate in the frame attached to the observation location will coincide with the rate of change of the radial coordinate in geocentric spherical coordinates. Because the debris particle's angular momentum is independent of $\dot{r}$, we find that the Delaunay variables G, H, and h will all be independent of $\dot{\rho}$. Because of this, zenith observations will have the property that $\mathbb{H}$ will have a constant zero eigenvector of $\langle 0,1\rangle$, throughout the admissible region $\mathcal{C}$. As a consequence of the above theorem, the reduced admissible region will be the intersection of the vertical line $\rho=\rho^*$ with the admissible region $\mathcal{C}$. We call the reduced admissible region $\mathcal{C}^r$ and likewise define

$$\mathcal{A}^r := \{\langle \rho,\dot{\rho},\alpha,\delta,\dot{\alpha},\dot{\delta}\rangle : (\alpha,\delta,\dot{\alpha},\dot{\delta}) = A \text{ and } (\rho,\dot{\rho}) \in \mathcal{C}^r\}$$

to be the (one-dimensional) admissible region of the observation space. By construction, the projection of $T(t;t_0)\{\mathcal{A}^r\}$ on the (H,h) plane will correspond to a single point: the intersection point as seen in Figs. 5 and 6. A similar statement can be made about $\mathcal{C}_{70}$ and $\mathcal{A}_{70}$, which are defined analogously for the second observation.

The reduced admissible regions $\mathcal{C}^r$ and $\mathcal{C}_{70}^r$ for the initial and second observations are plotted in Fig. 7. Their images under the transformation T, projected onto each of the three Delaunay planes, are shown in Fig. 8.

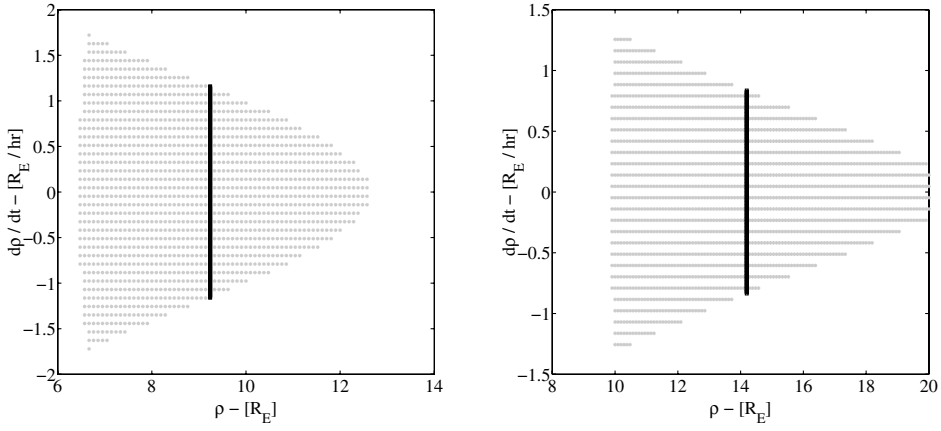

Fig. 7 $\mathcal{C}$ with $\mathcal{C}^r$ (dark or black), left panel; $\mathcal{C}_{70}$ with $\mathcal{C}_{70}^r$ (dark or black), right panel.

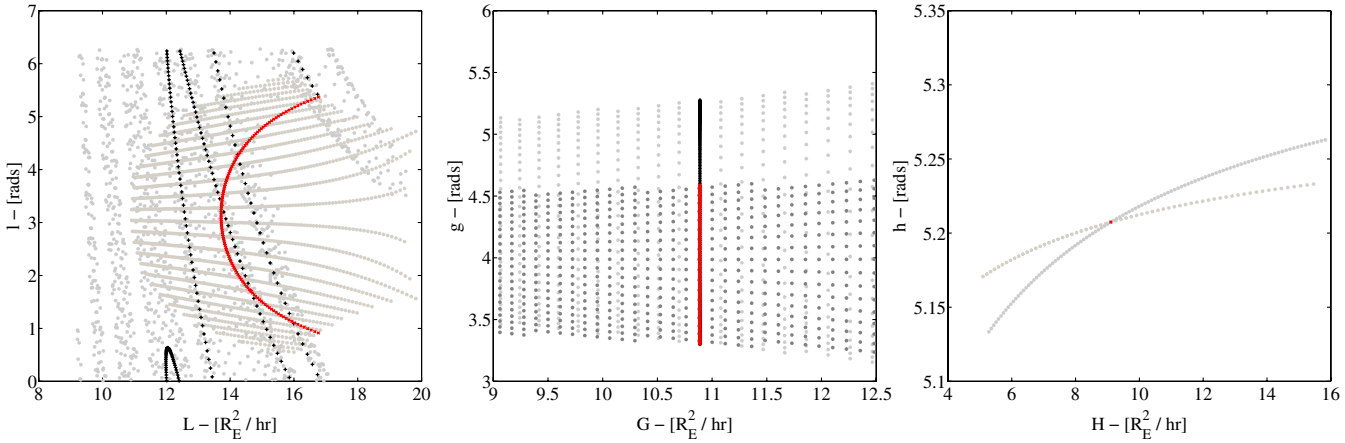

Fig. 8 Figure 5 plots with $T(70;0)\{\mathcal{A}^r\}$ (light or red) and $T(70;70)\{\mathcal{A}^r_{70}\}$ (dark or black).

C. Orbit Determination

By reducing the admissible regions $\mathcal{C}$ and $\mathcal{C}_{70}$ to the preimage of the intersection point on the (H, h) Delaunay plane, we found that the dimensionality of the admissible region can be reduced from 2 to 1. One can see that an additional reduction can be made by considering the projection of these curves on the (L, l) Delaunay plane, as seen in Fig. 8. These curves have five distinct intersection points on the (L, l) plane; therefore the actual uncertainty distribution has been reduced from a two-dimensional sheet to that of five distinct points in phase space. Additional information is also available from the overlap region of the two reduced curves as projected onto the (G, g) plane. In the case we are considering, only one of the five intersection points on the (L, l) plane actually lines up as an intersection point on the (G, g) plane. Therefore, the orbit is determined uniquely.

VI. Orbit Determination 2: Kepler Orbit With Two Near-Zenith Observations

In this section we study the case of two near-zenith observations. If the observation is not made when the space debris particle is directly overhead, the projection of the uncertainty region on the (H, h) plane will no longer be one dimensional. We will consider the same two attributable vectors that were observed in Sec. V, but nudge the inertial location of the observer so that the observations do not correspond to zenith observations. The first attributable vector is given by $A = (0\text{ rad}, \pi/6\text{ rad}, 0.1\text{ rad/h}, 0.03\text{ rad/h})$, made at time $t = 0$ h from a point on the Earth's surface $\Theta = \pi/3 + 0.1$ rad, $\Phi = 0.1$ rad. Assuming particle no. 1000 is the true space debris particle, a possible second observation (nonzenith) might be given by the attributable vector $A_{70} = (1.1516\text{ rad}, 0.4790\text{ rad}, 0.2262\text{ rad/h}, -0.0809\text{ rad/h})$, made at time $t = 70$ from a point on the Earth's surface $\Theta = 1.2516$ rad, $\Phi = 1.1918$ rad. The intersections of the admissible regions, as projected onto the Delaunay planes, are shown in Fig. 9. Because the true debris particle did not fly directly over zenith on either of the measurements, the admissible regions now have two-dimensional projections on the (H, h) plane. Because we are considering the Kepler case, the original uncertainty distribution's projections on the (G, g) and (H, h) plane are static. Our goal now is to systematically reduce the uncertainty region, by considering each Delaunay plane in sequence, as much as possible until it is reduced to either a single point (complete orbit determination) or a one-dimensional line.

By examination of the concurrent Delaunay plots of the uncertainty region projections (Fig. 9), we choose to begin the orbit determination process by cutting off the nonoverlap sections of the surface in the (H, h) plane. The Delaunay projections of the remaining piece of surface are shown in Fig. 10. We see in Fig. 10 that there is again an overlap and nonoverlap region in the (G, g) plane. Removing the nonoverlap region further reduces the admissible region, as shown in Fig. 11. Interestingly, the (H, h) projection can be again used to cut out more of the uncertainty surface, resulting in a third reduction, as shown in Fig. 12. We now turn to the projection of the thrice reduced uncertainty region on the (L, l) plane. The first three reductions have eliminated all but three overlap regions on the (L, l) plane. We consider each in term. The systematic projection of each overlap region onto each of the three Delaunay planes is shown in Fig. 13. We see that the far right overlap region on the (L, l) plane (the overlap that is almost confined to a single point) does not overlap on the (G, g) plane. This overlap region thus cannot correspond to the actual debris particle and is now ruled out. The middle overlap region on the (L, l) plane does not overlap on the (G, g) or (H, h) plane, so it is ruled out. Finally, the leftmost overlap region has a small intersection on both the (G, g) and (H, h) planes. The orbit is thus determined to within a small uncertainty about a single point in Delaunay space. It is possible that further reductions can be made by continuing this process: cut away the nonoverlap region of the (G, g) plane, then do the same for the new nonoverlap region of the (H, h) plane, and continue to

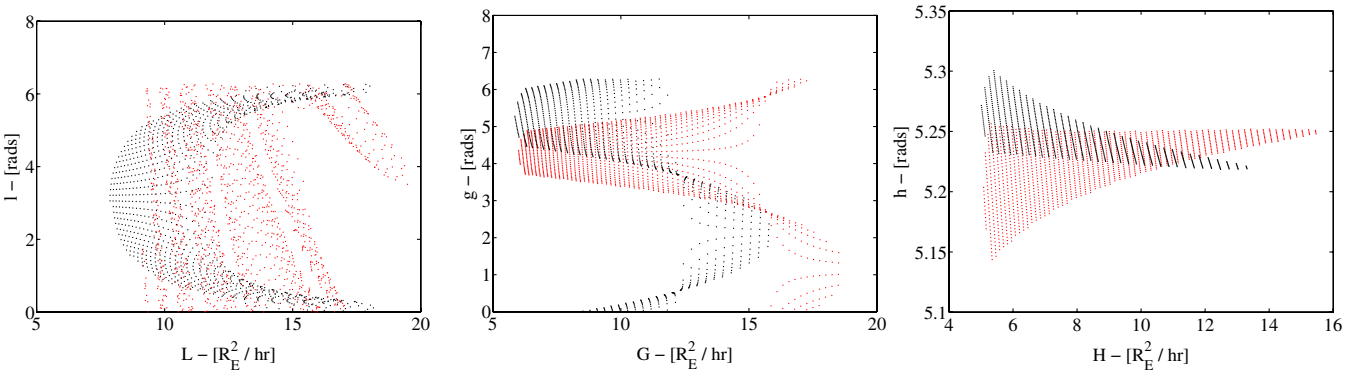

Fig. 9 $T(70;0)\{\mathcal{A}\}$ (light or red) and $T(70;70)\{\mathcal{A}_{70}\}$ (dark or black) projected onto the Delaunay planes, nonzenith observations.

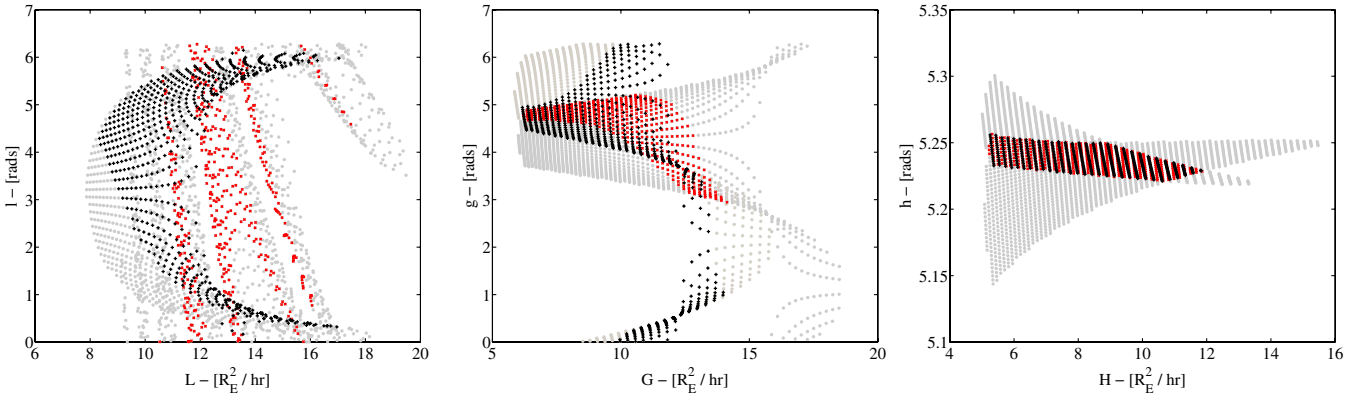

Fig. 10 $T(70;0)\{\mathcal{A}^r\}$ (light or red) and $T(70;70)\{\mathcal{A}^r_{70}\}$ (dark or black) projected onto the Delaunay planes, nonzenith observations.

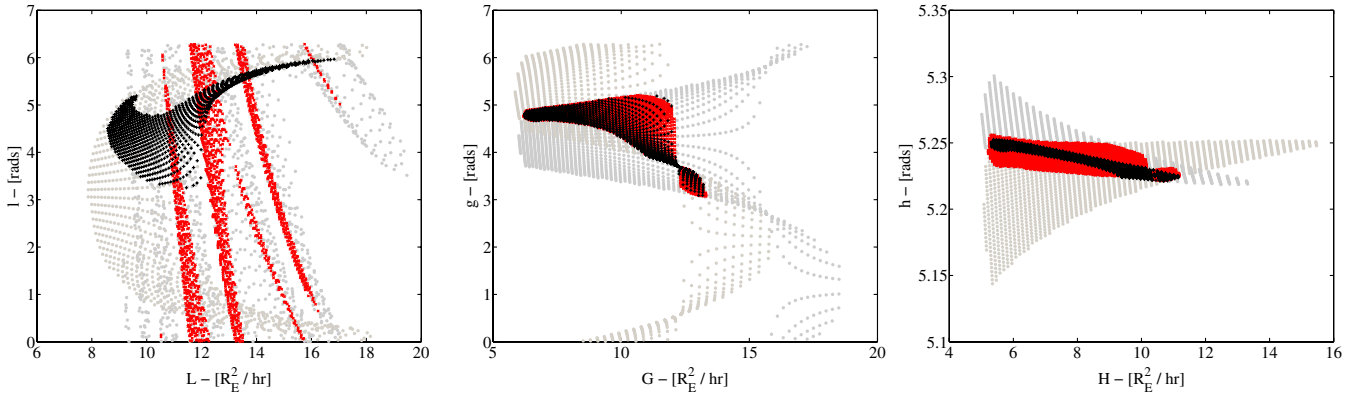

Fig. 11 $T(70;0)\{\mathcal{A}^{rr}\}$ (light or red) and $T(70;70)\{\mathcal{A}^{rr}_{70}\}$ (dark or black) projected onto the Delaunay planes, nonzenith observations.

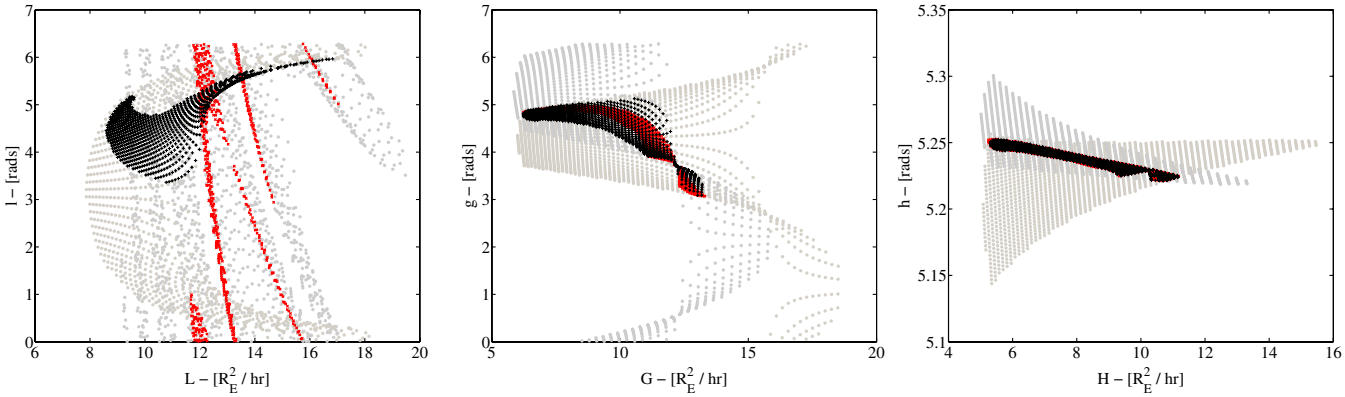

Fig. 12 $T(70;0)\{\mathcal{A}^{rrr}\}$ (light or red) and $T(70;70)\{\mathcal{A}^{rrr}_{70}\}$ (dark or black) projected onto the Delaunay planes, nonzenith observations.

ping-pong back and forth until the intersection is known to within the desired uncertainty. Alternatively, because the actual orbit is now known to within a small neighborhood of a single point, a least-squares solution can be carried out.

VII. Orbit Determination 3: J_2 Orbit

The intersection of two admissible regions (e.g,. Fig. 5) can take on a variety of different appearances. The purpose of this section is twofold. The main purpose is to present the reader with a menagerie of qualitatively different examples to give the reader a broader feel for how these overlap regions can appear. We will do this in the context of the J_2 problem, so that we can also show how the case where one treats perturbations differs from the associated Kepler problem.

A. Dynamics of the J_2 Orbit

It is known that the gravitational potential of an axisymmetric body can be expanded in a series of the form:

$$V = -\frac{GM}{r}\left(1 - \sum_{n=2}^{\infty} \frac{J_n P_n(\cos(\theta))}{r^n}\right)$$

where θ is measured from the axis of symmetry, and $P_n(x)$ is the nth Legendre polynomial. Taking into account the first-order correction of the gravitational field of the Earth, due to its oblateness, the potential can be approximated by

$$V \approx -\frac{\mu}{r} + \frac{\mu J_2(3\cos^2\theta - 1)}{r^2}$$

where μ is the gravitational parameter of the Earth and $J_2 \approx 1.08 \times 10^{-3}$ is the Earth's J_2 term. The disturbing function for the averaged

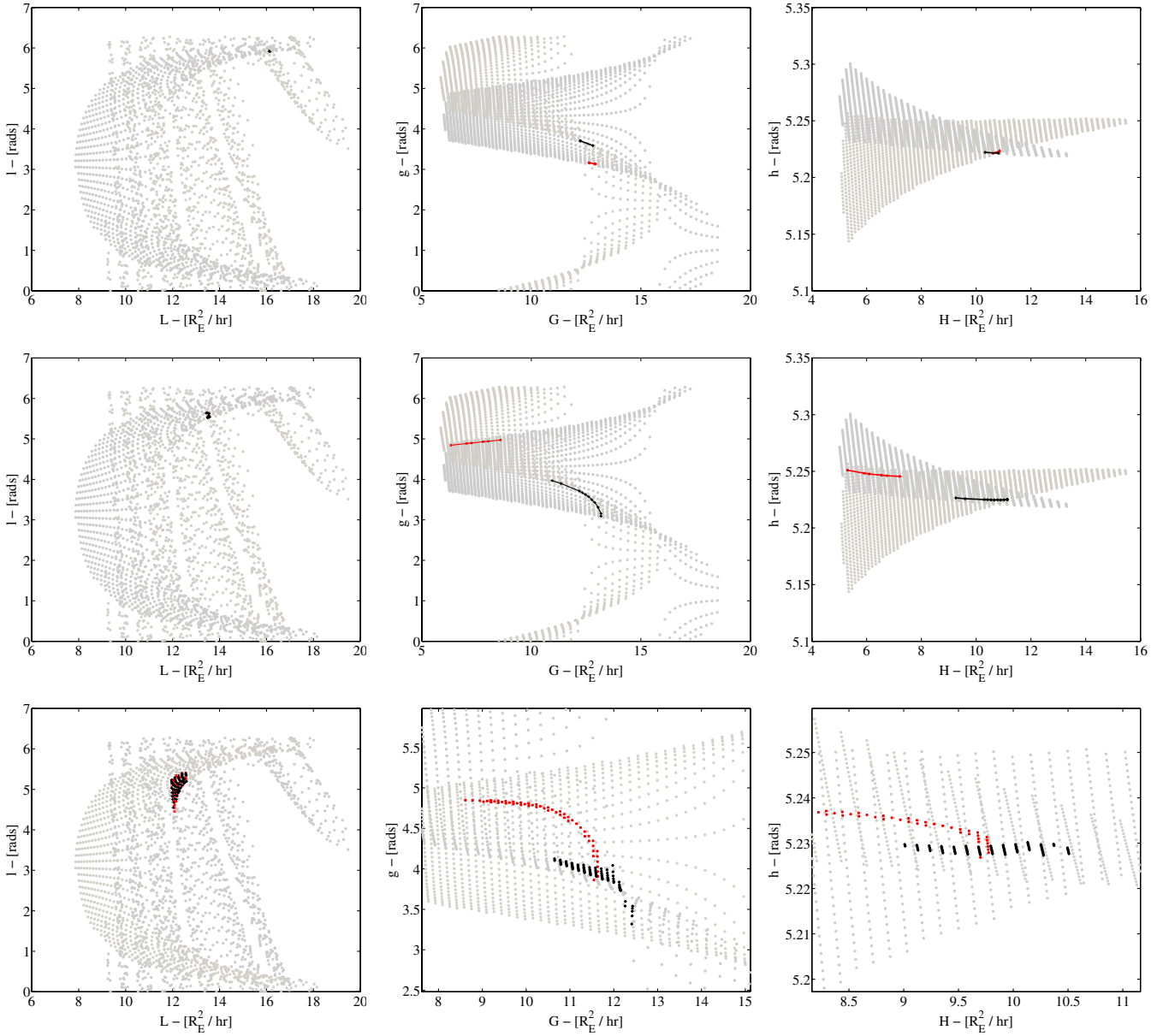

Fig. 13 $T(70;0)\{\mathcal{A}^{rrr}\}$ (light or red) and $T(70;70)\{\mathcal{A}^{rrr}_{70}\}$ (dark or black) projected onto the Delaunay planes, nonzenith observations.

potential for the J_2 problem can be written as [16]

$$R = \frac{\mu J_2}{2a^2(1-e^2)^{3/2}}\left(\frac{3}{2}\sin^2 i - 1\right)$$

The full Hamiltonian for the averaged J_2 problem can be written as

$$\mathcal{H} = -\frac{\mu}{2a} + \frac{\mu J_2}{2a^2(1-e^2)^{3/2}}\left(\frac{3}{2}\sin^2 i - 1\right)$$

Substituting the orbit elements with Delaunay variables (16), we can rewrite the potential as follows:

$$\mathcal{F} = -\frac{\mu^2}{2L^2} + \frac{\mu^4 J_2}{2L^3G^3}\left(\frac{1}{2} - \frac{3H^2}{2G^2}\right) \tag{23}$$

Applying Hamilton's equations (18) to the J_2 Hamiltonian (23), we obtain the following dynamic equations of motion for a particle in the Earth's J_2 field:

$$\frac{\mathrm{d}l}{\mathrm{d}t} = \frac{\mu^2}{L^3} - \frac{3\mu^4 J_2}{2L^4G^3}\left(\frac{1}{2} - \frac{3H^2}{2G^2}\right) \qquad \frac{\mathrm{d}g}{\mathrm{d}t} = \frac{15\mu^4 J_2 H^2}{4L^3G^6} - \frac{3\mu^4 J_2}{4L^3G^4}$$
$$\frac{\mathrm{d}h}{\mathrm{d}t} = -\frac{3\mu^4 J_2 H}{2L^3G^5} \tag{24}$$

The conjugate momenta are conserved:

$$\frac{\mathrm{d}L}{\mathrm{d}t} = 0 \qquad \frac{\mathrm{d}G}{\mathrm{d}t} = 0 \qquad \frac{\mathrm{d}H}{\mathrm{d}t} = 0$$

B. STM of the J_2 Dynamics

The STM corresponding to the transformation $T_4(t;t_0)$ will no longer be given by Eq. (21). The solution to the dynamic equations of motion (24) for the J_2 problem are simply

$$L(t) = L_0, \qquad G(t) = G_0, \qquad H(t) = H_0$$
$$l(t) = l_0 + \Lambda\cdot(t-t_0), \qquad g(t) = g_0 + \Gamma\cdot(t-t_0)$$
$$h(t) = h_0 + \Xi\cdot(t-t_0)$$

where we define

$$\Lambda = \frac{\mu^2}{L^3} - \frac{3\mu^4 J_2}{2L^4 G^3}\left(\frac{1}{2} - \frac{3H^2}{2G^2}\right) \qquad \Gamma = \frac{15\mu^4 J_2 H^2}{4L^3 G^6} - \frac{3\mu^4 J_2}{4L^3 G^4}$$

$$\Xi = -\frac{3\mu^4 J_2 H}{2L^3 G^5}$$

so that the STM is given by

$$\Phi_4^{J_2}(t;t_0) = \begin{bmatrix} 1 & 0 & 0 & 0 & 0 & 0 \\ \Lambda_L(t-t_0) & 1 & \Lambda_G(t-t_0) & 0 & \Lambda_H(t-t_0) & 0 \\ 0 & 0 & 1 & 0 & 0 & 0 \\ \Gamma_L(t-t_0) & 0 & \Gamma_G(t-t_0) & 1 & \Gamma_H(t-t_0) & 0 \\ 0 & 0 & 0 & 0 & 1 & 0 \\ \Xi_L(t-t_0) & 0 & \Xi_G(t-t_0) & 0 & \Xi_H(t-t_0) & 1 \end{bmatrix}$$

where Λ_L, Λ_G, and Λ_H are the partial derivatives of $\Lambda(L, G, H)$ with respect to L, G, and H, respectively, and similarly for Γ and Ξ.

C. Concurrent Plot of Two Zenith Observations on the Delaunay Planes

In this section we will assume the same initial observation of the debris particle as considered in Sec. V, that is, the attributable vector $A = (0 \text{ rad}, \pi/6 \text{ rad}, 0.1 \text{ rad/h}, 0.03 \text{ rad/h})$ is recorded at $t = 0$ h from the point $\Theta = \pi/3$ rad, $\Phi = 0$ rad, on the Earth's surface. The projections of the corresponding admissible region on the Delaunay planes are shown in Fig. 3. Taking into account the J_2 perturbation due to the Earth's oblateness on the debris particle's orbit, the time-evolved Delaunay projections are shown in Fig. 14. (The time-evolved Delaunay projections of the same admissible region in the Kepler case were shown in Fig. 4.) One sees that at these time scales, the J_2 effect on the (L, l) and (G, g) planes is fairly insignificant. On the (H, h) plane, the J_2 perturbation causes the projection of the uncertainty surface to widen from a line to a narrow two-dimensional region, thus regenerating the degenerate surface projection.

We consider now the three cases in which the actual debris particle is the virtual debris particles no. 400, no. 600, and no. 1000. Assuming a second zenith observation of the debris particle is made after 70 h; the two concurrent admissible region projections will appear as in Fig. 15. On the other hand, if the second observation is instead made after 140 h, the concurrent projections of the two admissible regions will appear as in Fig. 16. Notice that the projection of $T(t;0)\{A\}$ on the (L, l) plane becomes more shredded as it dynamically evolves. In fact, modulo the perturbations, most of the dynamical evolution of the original uncertainty surface is contained within this shredding. We show these cases to give the reader a broader feel of the variety in which these uncertainty intersections can appear. Because we treat the intersection procedure in Secs. V and VI, we will not discuss it again here.

VIII. A Conceptual Algorithm

The purpose of this paper has been to introduce and illustrate the viability of this orbit determination technique. As such, all surface intersection reductions were carried out by hand. Future research must be done on the development of technology that efficiently automates this process. As intersections of two-dimensional surfaces must be performed, and not higher-dimensional surfaces, it is feasible to develop computationally efficient approaches for this. In this section we discuss an algorithm and indicate how one might use this technology in the orbit determination process and the subsequent inclusion of these new orbits in the space debris catalog when faced with a large number of observations per night. As was mentioned in Sec. II.A, each observation should be recorded as an observation vector,

$$x = (A, t, L) \in \mathbb{R}^5 \times \mathbb{N}$$

that contains an attributable vector, the observation time, and the observatory's location. Each new observation should be checked against the catalog of known objects. If the observed attributable vector does not match any of the orbital particles in the catalog, it will be saved as an uncorrelated observation. A rolling observation window can be defined (for instance, one week) within which it is compared to all other uncorrelated observations. For these comparisons, a standard epoch time can be defined and all uncorrelated observations made within the observation window can then be mapped into the Delaunay planes and then dynamically evolved or regressed to the epoch time. These uncertainty projections can then be stored and intersected with all other such observations to discover which observations are correlated. For each orbit correlation that is found, the corresponding observations can then be saved in a secondary catalog, which is a temporary holding catalog, until the orbit is confirmed, at which time the data can be promoted to the primary catalog of correlated data.

IX. Alternative Approaches

As we discussed in Sec. IV.B, the correlation and orbit determination between two data tracks is tantamount to finding the unique intersection point $\mathbf{\Delta}^*$ of two two-dimensional submanifolds, $F^{\tau}_{\mathfrak{X}_1}(\mathcal{C}_1)$ and $F^{\tau}_{\mathfrak{X}_2}(\mathcal{C}_2)$, of six-dimensional Delaunay space $\mathcal{D} \cong \mathbb{R}^6$. It is the scope of this paper to discuss the feasibility of an approach, presented in this current work, known as the intersection theory analysis. The ITA algorithm was introduced in Sec. IV.C and further illustrated by means of example in Secs. V, VI, and VII, for the cases of zenith observations, near-zenith observations, and J_2 orbital perturbations, respectively. In this current section we will discuss some viable alternative approaches for determining the intersection point $\mathbf{\Delta}^*$, thus obtaining an orbit determination. A thorough analysis of these alternative approaches will be the study of future research; it is our goal here only to demonstrate the voracity of a subvolume intersection approach to orbit determination problems, in the sense

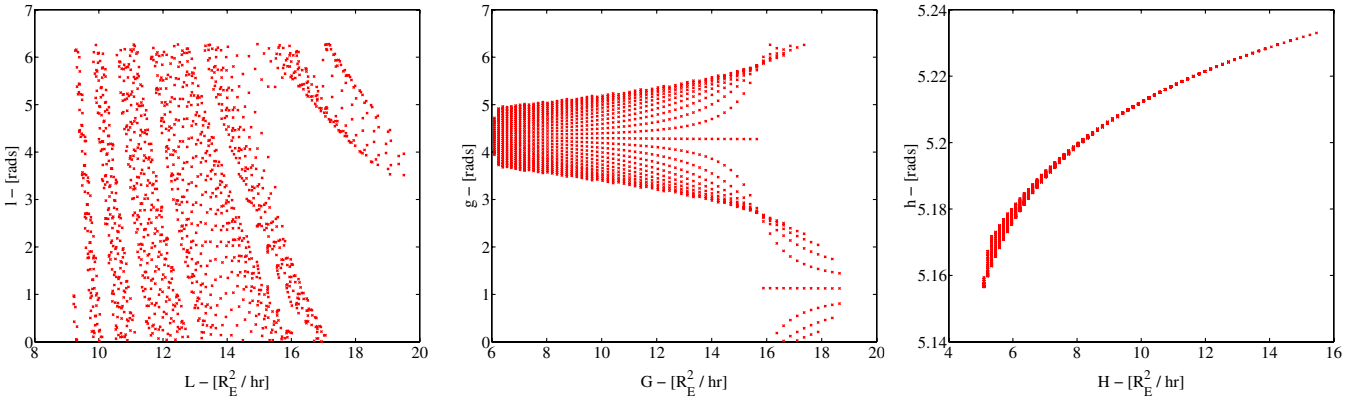

Fig. 14 $T(70;0)\{\mathcal{A}\}$ projected onto the Delaunay planes, J_2 problem.

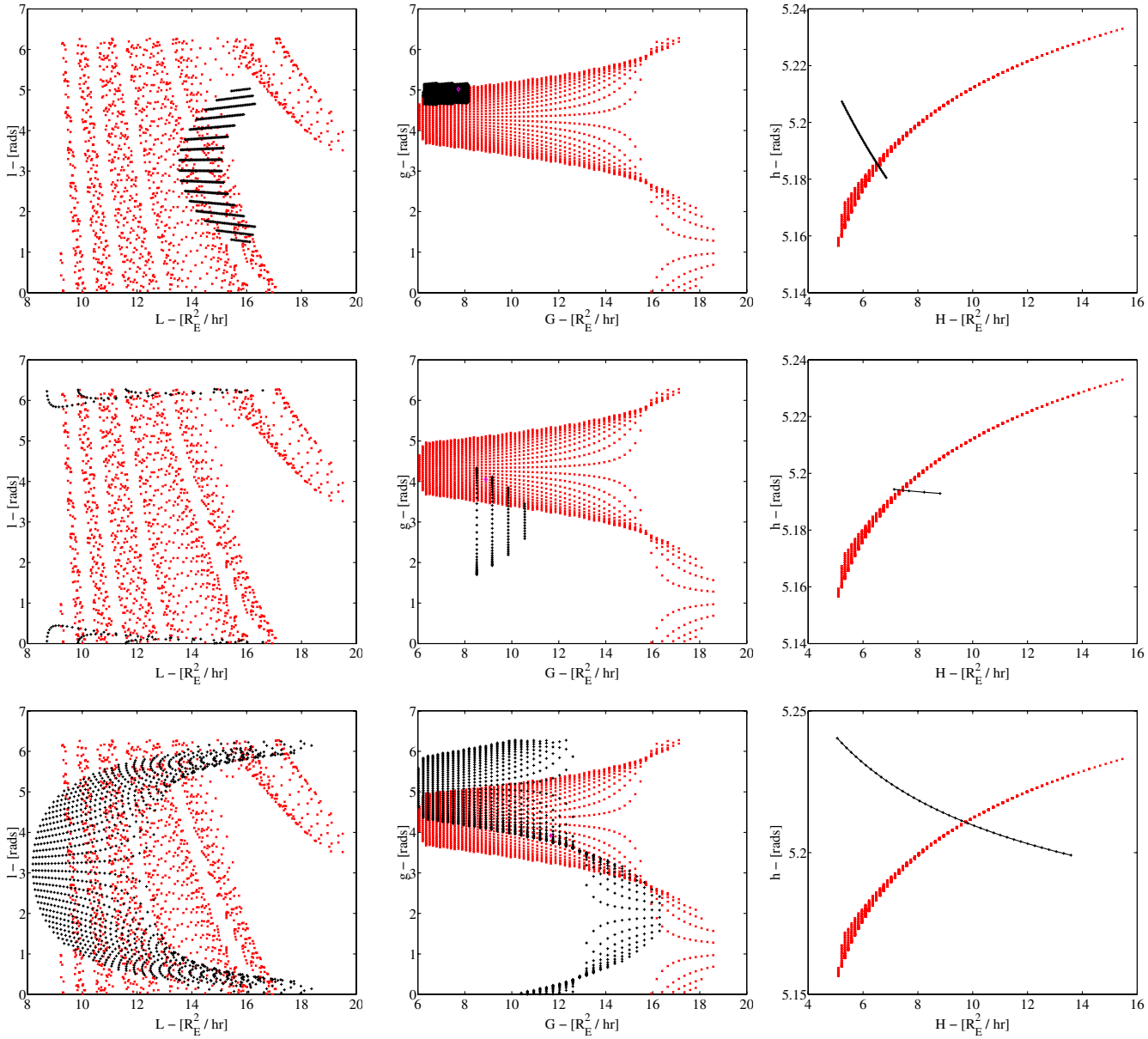

Fig. 15 $T(70;0)\{\mathcal{A}\}$ **(light or red) and** $T(70;70)\{\mathcal{A}_{70}\}$ **(dark or black) projected onto the Delaunay planes,** J_2 **problem. Assumes the true particle is no. 400, no. 600, and no. 1000, from top down.**

that there are competing methodologies within this approach, each with its own merits, that could lead to fruitful results.

A. Topocentric Intersection Theory Analysis

The first alternative approach we shall discuss is topocentric intersection theory analysis (TITA). As the name suggests, TITA involves performing the same intersection theory analysis routine in the topocentric observation geometry as opposed to the Delaunay space. As the topocentric viewing geometry is continuously transforming, there is no common space in which to compare all uncertainty distributions. Instead, for each pair of tracks, one does the following. First compute the admissible region corresponding to each track of data. Pull the second admissible regions back into geocentric Cartesian coordinates, dynamically map the resulting distribution forward or backward in time to the time of the first track, and then push the resulting manifold forward to the topocentric coordinates in which the first track was viewed. This approach has the possible disadvantage that *for each pair* of tracks, an uncertainty surface must be mapped into a new space, entailing a total of $O(N^2)$ surface mappings for a set of N uncorrelated tracks. Recall that for regular ITA, each uncertainty surface is *mapped once* into a common space for comparison, yielding a total of $O(N)$ such mappings. In the TITA approach, one then carries out the ITA algorithm in the topocentric observation projective spaces $\mathcal{O}_\rho = (\rho, \dot{\rho})$, $\mathcal{O}_\alpha = (\alpha, \dot{\alpha})$, and $\mathcal{O}_\delta = (\delta, \dot{\delta})$. TITA has the advantage that *one* of the uncertainty surfaces degenerates to a single point in the projective spaces $\mathcal{O}_\alpha$ and $\mathcal{O}_\delta$. Thus, ITA degenerates to checking to see if the second uncertainty manifold contains in it a four-vector $\boldsymbol{\theta} = \langle \alpha, \dot{\alpha}, \delta, \dot{\delta} \rangle$ in an epsilon neighborhood of the original attributable vector A of the first observation. If so, one then checks to see if the corresponding $\langle \rho, \dot{\rho} \rangle$ of the second uncertainty surface lie on the admissible region of the first. Thus the ease with which one performs ITA in the topocentric projective space and added computation associated with the additional surface mappings must be compared with the relative complexity in performing intersections in the Delaunay projective spaces and the associated computational advantage of performing fewer surface mappings.

B. Metric Approaches

As the ultimate goal is to find the intersection point shared by two two-dimensional surfaces $F^{\tau}_{\mathfrak{X}_1}(\mathcal{C}_1)$ and $F^{\tau}_{\mathfrak{X}_2}(\mathcal{C}_2)$, each represented by a discretized VD field mapped to Delaunay space, a natural approach

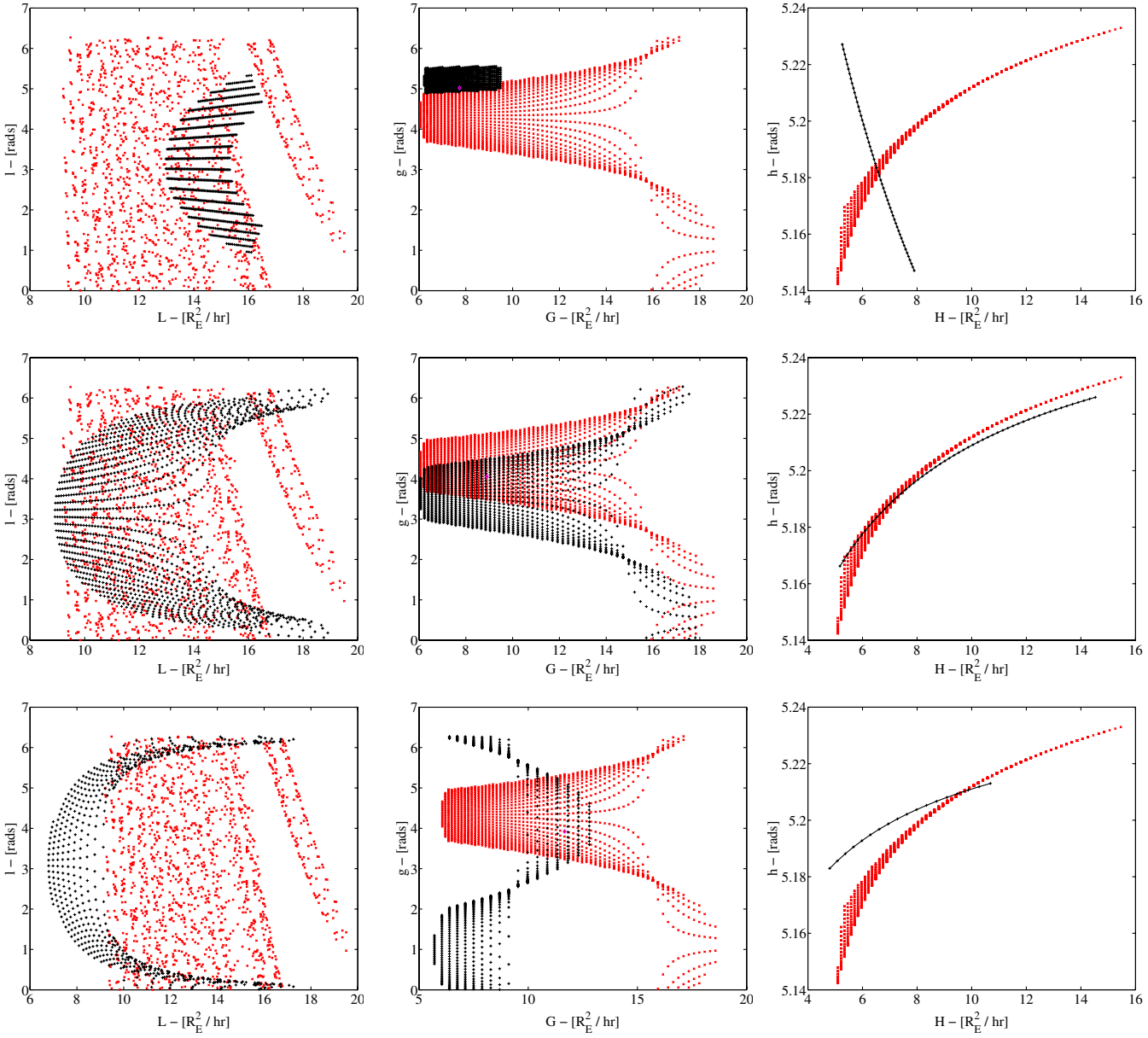

Fig. 16 $T(140;0)\{\mathcal{A}\}$ **(light or red) and** $T(140;140)\{\mathcal{A}_{70}\}$ **(dark or black) projected onto the Delaunay planes,** J_2 **problem. Assumes the true particle is no. 400, no. 600, and no. 1000, from top down.**

might be to find the pair of points $\boldsymbol{\Delta}_1^* \in F^{\tau}_{\mathfrak{X}_1}(\mathcal{C}_1)$ and $\boldsymbol{\Delta}^* \in F^{\tau}_{\mathfrak{X}_2}(\mathcal{C}_2)$ which are "closest together" in some sense. The accomplishment of this objective depends on the suitable choice of a metric for the Delaunay space $\mathcal{D}$. Taking the example of two zenith observations considered in Sec. V, there are literally hundreds of point pairs, $\{\boldsymbol{\Delta}_{1i} \in F^{\tau}_{\mathfrak{X}_1}(\mathcal{C}_1); \boldsymbol{\Delta}_{2i} \in F^{\tau}_{\mathfrak{X}_2}(\mathcal{C}_2)\}_{i=1}^{100's}$, whose Euclidean separation distance $\|\boldsymbol{\Delta}_{1i} - \boldsymbol{\Delta}_{2i}\|_{\text{Euclid}}$ is less than the distance between the actual approximate intersection points $\boldsymbol{\Delta}_1^*$ and $\boldsymbol{\Delta}_2^*$ yielded by ITA and known to be correct by construction. Many of these false positives do not even hit the obvious intersection point on the (H, h) plane (see Fig. 5). Clearly a much more judicious choice of metric is needed. One could imagine that with the correct metric, the pair of points that lies closest together will always be the intersection point. Such a discovery would greatly reduce the computational complexity of repeatedly performing successive intersections between overlapping planar laminas.

Typically when one speaks of a metric one thinks of it as being defined globally, that is, we would have

$$\mathbf{g}: T\mathcal{D} \times T\mathcal{D} \to \mathbb{R}$$

We will, however, require a metric $\mathbf{g}_1$ that is defined only on the restriction of $\mathcal{D}$ to the submanifold $F^{\tau}_{\mathfrak{X}_1}(\mathcal{C}_1)$, so that

$$\mathbf{g}_1: T\mathcal{D}|_{F^{\tau}_{\mathfrak{X}_1}(\mathcal{C}_1)} \times T\mathcal{D}|_{F^{\tau}_{\mathfrak{X}_1}(\mathcal{C}_1)} \to \mathbb{R}$$

Note $\mathbf{g}_1$ takes as inputs full six-dimensional vectors from $T\mathcal{D}$, only it is defined solely at points located on the submanifold $F^{\tau}_{\mathfrak{X}_1}(\mathcal{C}_1)$; it is *not* the tangent bundle to this submanifold. For any point $\boldsymbol{\Delta}_1 \in F^{\tau}_{\mathfrak{X}_1}(\mathcal{C}_1)$, the metric $\mathbf{g}_1(\boldsymbol{\Delta}_1)$ is a good approximation for the metric in a local neighborhood $\mathcal{U} \subset \mathcal{D}$ of $\boldsymbol{\Delta}_1$. Thus for any $\boldsymbol{\Delta} \in \mathcal{U}$, the distance between $\boldsymbol{\Delta}$ and $\boldsymbol{\Delta}_1$ is approximated by

$$d(\boldsymbol{\Delta}, \boldsymbol{\Delta}_1) \approx \sqrt{(\boldsymbol{\Delta} - \boldsymbol{\Delta}_1)^T \cdot \mathbf{g}_1(\boldsymbol{\Delta}_1) \cdot (\boldsymbol{\Delta} - \boldsymbol{\Delta}_1)}$$

However, if the point $\boldsymbol{\Delta}$ is far away, we care less about the actual measure of this distance than about the fact that it is far away. Hence one can simply seek the points $\boldsymbol{\Delta}_1^*$ and $\boldsymbol{\Delta}_2^*$ that minimize

$$D_{\min} = \inf_{\mathbf{\Delta}_1 \in F^{\tau}_{\mathfrak{x}_1}(\mathcal{C}_1)} \left[\inf_{\mathbf{\Delta}_2 \in F^{\tau}_{\mathfrak{x}_2}(\mathcal{C}_2)} \left(\sqrt{(\mathbf{\Delta}_2 - \mathbf{\Delta}_1)^T \cdot \mathbf{g}_1(\mathbf{\Delta}_1) \cdot (\mathbf{\Delta}_2 - \mathbf{\Delta}_1)} \right) \right]$$

Because both submanifolds are discretized by VD fields, one simply compares this quantity for pairwise sets of points.

As mentioned previously, the successful actualization of this method depends on the correct choice of metric $\mathbf{g}_1$. Such a metric might be constructed as to preserve the integrity and structure of the observation geometry in which the attributable vector was first recorded. The Euclidean metric induces the following metric on the spherical coordinates $\langle \rho, \dot{\rho}, \alpha, \delta, \dot{\alpha}, \dot{\delta} \rangle$ used in the topocentric (TC) frame:

$$\mathbf{g}_{\mathrm{TC}} = \begin{pmatrix} 1 & 0 & 0 & 0 & 0 & 0 \\ 0 & 1 & 0 & 0 & 0 & 0 \\ 0 & 0 & \rho \cos\delta & 0 & 0 & 0 \\ 0 & 0 & 0 & \rho & 0 & 0 \\ 0 & 0 & 0 & 0 & \rho \cos\delta & 0 \\ 0 & 0 & 0 & 0 & 0 & \rho \end{pmatrix}$$

One can simply push this metric forward to Delaunay space in the following sense. For any $\mathbf{\Delta} \in F^{\tau}_{\mathfrak{x}_1}(\mathcal{C}_1)$ and $\mathbf{v}_1, \mathbf{v}_2 \in T_{\mathbf{\Delta}}\mathcal{D}$, define

$$\mathbf{g}_1(\mathbf{\Delta})(\mathbf{v}_1, \mathbf{v}_2) = \mathbf{g}_{\mathrm{TC}}\left(F^{\tau -1}_{\mathfrak{x}_1}(\mathbf{\Delta})\right)\left(\left(\mathrm{d}F^{\tau}_{\mathfrak{x}_1}\right)^{-1} \cdot \mathbf{v}_1, \left(\mathrm{d}F^{\tau}_{\mathfrak{x}_1}\right)^{-1} \cdot \mathbf{v}_2\right)$$

Because the matrix of the linear transformation $\mathrm{d}F^{\tau}_{\mathfrak{x}_1}$ is simply the Jacobian matrix Φ of the transformation, the computation of which was discussed in Sec. III.B, which is easily computed, we have

$$\begin{aligned} \mathbf{g}_1(\mathbf{\Delta})(\mathbf{v}_1, \mathbf{v}_2) &= \mathbf{g}_{\mathrm{TC}}\left(F^{\tau -1}_{\mathfrak{x}_1}(\mathbf{\Delta})\right)(\Phi^{-1} \cdot \mathbf{v}_1, \Phi^{-1} \cdot \mathbf{v}_2) \\ &= \mathbf{v}_1^T \cdot (\Phi^{-1})^T \cdot \mathbf{g}_{\mathrm{TC}} \cdot \Phi^{-1} \cdot \mathbf{v}_2 \end{aligned}$$

The matrix of the metric $\mathbf{g}_1$ is given by

$$\mathbf{g}_1 = (\Phi^{-1})^T \cdot \mathbf{g}_{\mathrm{TC}} \cdot \Phi^{-1}$$

This approach is not as of yet entirely robust, as it still returns false positives for the intersection point. However, it seems to preserve the visual sense of closeness one has from visual examination of the Delaunay planes, that is, points close together actually look close together. This has not always been the case with other metrics we experimented with. Further investigation and development of this metric will be a topic of future research.

X. Conclusions

This work is a preliminary study in which we propose a new conceptual procedure for carrying out orbit determination of space debris from two previously uncorrelated tracks observed with optical telescopes. We show how an optical track can be reduced to a four-dimensional estimate of the substate and how the mapping of the admissible region into Delaunay space can be used to construct a notional algorithm for computing an orbit correlation and determination between two uncorrelated tracks. Our approach reduces the orbit correlation and determination process to performing intersections of two-dimensional laminas in the plane, a process we call intersection theory analysis. For an example attributable vector we carry out this process as a proof-of-concept computation for both a zenith and near-zenith observation. For the case of a zenith observation, a degeneracy in the viewing geometry simplifies this computation as the projection of the admissible surface onto the third Delaunay plane is simply a line (as opposed to a lamina). For the near-zenith observations this degeneracy disappears, but an orbit determination can nonetheless be performed using the same process; we therefore believe that there will be no additional difficulty in carrying out this process for nonzenith observations.

References

[1] Rossi, A., "Population Models of Space Debris," *Dynamics of Population of Planetary Systems, Proceedings of IAU Colloquium*, edited by A. Milani and Z. Knežević, Cambridge Univ. Press, New York, Vol. 197, 2005, pp. 427–438.

[2] Rossi, A., "The Earth Orbiting Space Debris," *Serbian Astronomical Journal*, No. 170, 2005, pp. 1–12. doi:10.2298/SAJ0570001R

[3] Tommei, G., Milani, A., and Rossi, A., "Orbit Determination of Space Debris: Admissible Regions," *Celestial Mechanics and Dynamical Astronomy*, Vol. 97, No. 4, 2007, pp. 289–304. doi:10.1007/s10569-007-9065-x

[4] Milani, A., Gronchi, G., Vitturi, M., and Knežević, Z., "Orbit Determination with Very Short Arcs. IAdmissible Regions," *Celestial Mechanics and Dynamical Astronomy*, Vol. 90, No. 1, 2004, pp. 57–85. doi:10.1007/s10569-004-6593-5

[5] Delaunay, C., "Theorie du Mouvement de la Lune," *Memoires de l'Academie des Sciences*, Vol. 28, 1860.

[6] Delaunay, C., "Theorie du Mouvement de la Lune," *Memoires de l'Academie des Sciences*, Vol. 29, 1867.

[7] Born, M., *The Mechanics of the Atom*, G. Bells and Sons, Ltd, London, 1927, pp. 36–44.

[8] Abraham, R., and Marsden, J. E., *Foundations of Mechanics*, 2nd ed., Addison–Wesley, Reading, MA, 1978, pp. 206–230.

[9] Brouwer, D., and Clemence, G. M., *Methods of Celestial Mechanics*, Academic Press, New York, 1961, pp. 273–291.

[10] Chang, D. E., and Marsden, J. E., "Geometric Derivation of the Delaunay Variables and Geometric Phases," *Celestial Mechanics and Dynamical Astronomy*, Vol. 86, No. 2, 2003, pp. 185–208. doi:10.1023/A:1024174702036

[11] Maruskin, J. M., Scheeres, D. J., and Bloch, A. M., "SubVolumes in Dynamical Systems and the Tracking of Space Debris," *The Proceedings of the 2007 AAIA/AAS Astrodynamics Specialist Conference*, AIAA, Reston, VA, 2007, pp. 2223–2243; also AAS Paper 07-392.

[12] Seitzer, P., Smith, R., Africano, J., Jorgensen, K., Stansbery, E., and Monet, D., "MODEST Observations of Space Debris at Geosynchronous Orbit," *Advances in Space Research* Vol. 34, No. 5, 2004, pp. 1139–1142. doi:10.1016/j.asr.2003.12.009

[13] Milani, A., and Knežević, Z., "From Astronomy to Celestial Mechanics: Orbit Determination with Very Short Arcs," *Celestial Mechanics and Dynamical Astronomy*, Vol. 92, No. 1, 2005, pp. 1–18. doi:10.1007/s10569-005-3314-7

[14] Hamilton, T. W., and Melbourne, W. G., "Information Content of a Single Pass of Doppler Data from a Distant Spacecraft," JPL-SPS 37–39, Vol. 3, 31 May 1966, pp. 18–23.

[15] Crassidis, J. L., and Junkins, J. L., *Optimal Estimation of Dynamic Systems*, Chapman & Hall/CRC, Boca Raton, FL, 2004, pp. 159–164.

[16] Danby, J. M. A., *Fundamentals of Celestial Mechanics*, Willmann-Bell, Richmond, VA, 1988, pp. 125–138, 201–206.

[17] Montenbruck, O., and Gill, E., *Satellite Orbits: Models, Methods, Applications*, Springer, New York, 2000, pp. 28–29.

[18] Roy, A. E., *Orbital Motion*, Institute of Physics, Bristol, 1988, pp. 70–105.

[19] Ferraz-Mello, S., *Canonical Perturbation Theories: Degenerate Systems and Resonance*, Springer, New York, 2007, p. 1.

[20] Montenbruck, O., and Gill, E., *Satellite Orbits: Models, Methods, Applications*, Springer, New York, 2000, pp. 235–239.

[21] Maruskin, J. M., Scheeres, D. J., and Bloch, A. M., "Dynamics of Symplectic SubVolumes," *Journal of Applied Dynamical Systems* (to be published).

[22] Arnold, V. I., *Mathematical Methods of Classical Mechanics*, 2nd ed., Springer–Verlag, Berlin, 1978, pp. 206–207.

[23] Scheeres, D. J., Hsiao, F. Y., Park, R. S., Villac, B. F., and Maruskin, J. M., "Fundamental Limits on Spacecraft Orbit Uncertainty and Distribution Propogation," *Journal of the Astronautical Sciences*, Vol. 54, Nos. 3–4, 2006, pp. 505–523.